Fine to coarse mesh transition in phase-field fracture simulations using the virtual element method

Shubham Sharma, Himanshu, Ananth Ramaswamy*

Department of Civil Engineering, Indian Institute of Science, Bengaluru, Karnataka 560012, India

Abstract

In this study, the virtual element method (VEM) is utilized to address fine-to-coarse mesh transitions in phase-field fracture simulations for brittle, homogeneous media. The VEM discretization of the phase-field brittle damage equation is proposed, where the consistency and stability matrices of the damage sub-problem are derived by treating it as a general second-order linear elliptic equation. A nodal average phase-field measure is introduced to compute the degraded stress field for the elasticity subproblem. This leads to an explicit dependence of the elasticity stability matrix on the phase-field variable. A refinement strategy based on the analytical displacement fields of linear elastic fracture mechanics (LEFM) is proposed to give some guidelines on the number and positioning of hanging nodes relative to the crack front. The proposed discretization strategy is benchmarked against numerical simulations using the finite element method (FEM), smoothed finite element method (SFEM), and experimental results to demonstrate its robustness. The coupled equations for damage and displacement field is solved using a staggered algorithm implemented in the commercial software Abaqus (Standard). A Static Adaptive Mesh Refinement (SAMR) strategy is also implemented in Abaqus (Standard) to highlight the ease with which VEM can be used in phase-field fracture simulations when the crack path is not known *a priori*. The versatility of the strategy can lead to the efficient treatment of hanging nodes in adaptive mesh refinement (AMR) and global-local approaches, as well as enable efficient and accurate phase-field fracture simulations in large-scale engineering structures.

Keywords: Virtual element method (VEM), phase-field, Global-local approach, hanging nodes

1. Introduction

Numerical simulations of a crack propagating in a solid continuum continue to be an active area of research. Accurate prediction of material failure through fracture simulations is critical for ensuring the reliability and safety of engineering structures. Traditional approaches, such as the cohesive zone model [5], extended finite element method [53] often

*Corresponding author

Email address: ananth@iisc.ac.in (Ananth Ramaswamy)

struggle to capture the complexity of crack propagation, particularly in cases of branching, coalescence, and multi-crack interactions. The phase-field method (PFM) has emerged as a robust framework for simulating fracture, owing to its ability to represent cracks implicitly as a diffuse interface without requiring explicit tracking of crack surfaces. This makes PFM highly versatile for a wide range of fracture scenarios, including dynamic crack branching and complex geometries, where traditional methods face significant challenges [8, 37]. However, one of the key limitations of the phase-field approach is its necessity for a very fine mesh resolution near crack tips to accurately capture sharp gradients in the stress field and the phase-field variable. This requirement significantly increases the computational cost, especially for large-scale [48, 35] or three-dimensional simulations [62].

In large-scale phase-field simulations for engineering structures, where vast computational domains are involved, it is computationally beneficial to have a fine mesh resolution near cracks while maintaining a coarse mesh in the adjoining regions. However, this leads to an increased number of transition elements while transitioning from a very fine mesh to a coarse mesh. Fine-to-coarse mesh transitions become essential in such scenarios, allowing for localized refinement in regions where the crack is expected to propagate while maintaining a coarser mesh in less critical regions. This selective refinement drastically reduces the computational burden, enabling the simulation of large, complex structures such as dams, bridges, aircraft components, or pipelines, where crack initiation and propagation can occur over extended periods and locations. This can enable engineers to employ phase-field damage models to simulate crack initiation and propagation in large domains without sacrificing the accuracy needed near the crack tip, where the solution is most sensitive.

Techniques such as adaptive mesh refinement (AMR) [4, 45, 24, 38] and global-local approaches [40, 23] are commonly employed to manage the balance between accuracy and computational efficiency. However, these techniques often lead to the generation of non-conforming meshes, introducing hanging nodes at the interface of fine and coarser regions. Another challenge, specifically in AMR schemes, is the frequent re-meshing, which is a time-consuming and computationally tedious process, as it involves multiple additional operations at each convergence iteration, such as checking refinement criteria, mesh smoothing, updating element connectivity, and transferring variables between mesh configurations [11]. Often, multiple refinement cycles may be needed within a single increment step, significantly increasing the computational burden. Furthermore, the implementation of user-defined AMR schemes is limited to in-house developed codes, and their implementation in commercial finite element software such as Abaqus [17] is rather not straightforward.

Hanging nodes are considered a variational crime [51] in traditional Finite Element Methods (FEM), as they pose significant convergence difficulties and complicate the enforcement of continuity and compatibility between adjacent meshes. Several methods exist in the literature to address the problem of hanging nodes. Various methods have been adopted in the AMR schemes and global-local approaches used in phase-field fracture simulations. These include multiscale basis functions [64, 63, 41], Nitsche's method [49, 50], dual mortar method [60, 46, 44, 40, 2], among others. Despite the effectiveness of these methods in handling hanging nodes, they all require special treatments to ensure continuity across non-conforming meshes, which often leads to increased computational complexity. Alterna-

tively, the polygonal finite element methods (PFEM), do not require special treatment for hanging nodes [54, 56], naturally accommodating non-conforming meshes without the need for additional constraints or modifications. PFEM and its variants such as the smoothed-finite element method (SFEM) [32] have been used in AMR schemes in phase-field fracture simulations in [45, 31, 24, 55, 42, 59, 25]. However, the use of polygonal finite elements requires the computation of finite element shape functions and the numerical integration schemes over these elements can be non-trivial.

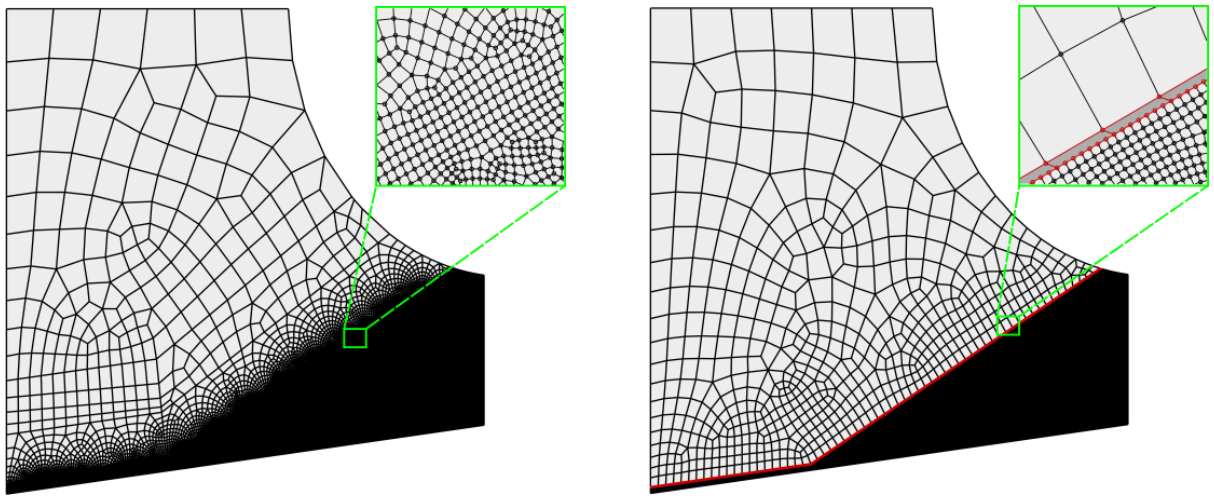

(a) (b)

Figure 1: Comparison of the number of elements generated in the coarse mesh (light grey) region (a) FEM mesh generated in ABAQUS (4764 elements) (b) VEM mesh (623 elements)

In contrast, the virtual element method (VEM), introduced in the seminal work of [57], provides a robust yet elegant solution for the treatment of hanging nodes in the interface between fine and coarse mesh. VEM bridges the mimetic finite differences (MFD) and FEM by implicitly defining trial and test functions within a conforming Galerkin framework, allowing for geometric flexibility like MFD while maintaining the variational structure of FEM. The essential ingredient of VEM is the projection operator [58], which computes the bilinear form without constructing the shape functions. Its flexibility in handling arbitrary (convex or non-convex) polygonal or polyhedral meshes, without the need for complex shape function construction gives it a clear advantage over existing methods. VEM has been used to solve a myriad range of problems such as linear elasticity [14, 21, 36], finite deformation [12], plasticity [15], damage [18, 39], computational homogenization [9], contact problems [61, 13], phase-field fracture simulations [1, 33], fracture of heterogeneous materials and polycrystalline composites [47, 6, 22], hydrogen-assisted cracking [34], amongst others. In [1], a monolithic scheme was used to solve the phase-field fracture equations. However, the stability term was constructed by triangulating the polygonal elements and assuming a linear variation within each subdomains. In [34, 33], a staggered scheme was adopted for the phase-field fracture for solving hydrogen-assisted and dynamic fracture problems. However, the formulation employed certain assumptions such as the use of average damage gradient

over the element and avoiding the dependence of the phase-field variable while computing the stability term for the elasticity subproblem.

Additionally, limited studies have been done that emphasize the VEM's ability to deal with a large number (> 2) of hanging nodes in phase-field brittle fracture simulations. VEM's flexibility in dealing with hanging nodes was used in an AMR and mesh cutting scheme for phase-field brittle fracture simulations in [26]. However, the mesh refinement scheme used only triangular and polygonal elements with no more than 2 hanging nodes. Furthermore, little emphasis was given to the position and number of hanging nodes that can be allowed without a loss of accuracy in the mesh. Interestingly, in [52] the stiff inclusion in a matrix was discretised using a single virtual element with a large number of hanging node. However, the study was only limited to a linear elastic analysis. Even in the absence of AMR schemes in phase-field fracture simulations, VEM's ability to naturally deal with hanging nodes can be exploited to keep a very fine mesh in the desired region while maintaining a coarse mesh in adjoining regions. This is illustrated in Fig. 1 where a complicated geometry is meshed using finite elements (Fig. 1a) and virtual elements (Fig. 1b). Using elements with 6 hanging nodes, the number of elements in the coarse mesh region can be drastically reduced by up to 85 percent as compared to conventional FEM which uses only quadrilaterals of varying sizes to make such a transition. Thus, a systematic and rigorous study on the use of hanging nodes to achieve a fine to coarse mesh transition in pre-refined domains forms a motivation of the current study. The key contributions of this work are

- A simple and robust VEM discretization of the damage and elasticity sub problems for the phase-field brittle damage theory in a homogeneous, isotropic medium.
- A novel refinement strategy to fix the position and number of elements with hanging nodes using the concept of K-field loading of LEFM.
- Highlighting VEM's superiority in terms of reduced number of degrees of freedom and computational time with respect to FEM and SFEM using benchmark simulations.
- Validation with experimental results of a specimen undergoing mixed mode fracture with the numerical simulations of a domain discretised with elements having large number of hanging nodes.

The remainder of this paper is organized as follows. In Section 2, the governing equations of the phase-field damage theory are derived using the principle of virtual power. Section 3 gives details on the VEM discretizations of the damage and elasticity sub-problems. A strategy to fix the number and position of elements with hanging nodes, along with comparisons with numerical benchmarks and experimental validations, is given in Section 4. Finally, Section 5 concludes the study with a summary of key findings and suggestions for future work.

2. Phase-field modeling of brittle fracture

Consider a solid body in the reference configuration, $\Omega \subset \mathbb{R}^{\delta}$ with dimension $\delta \in [2, 3]$ and $\partial\Omega \subset \mathbb{R}^{\delta-1}$ be its boundary. We intend to describe the deformation of the body as it

undergoes fracture with time. Thus, for a material point $\mathbf{X} \in \Omega$ and time $t \in \mathcal{T} \subset \mathbb{R}$ we define the displacement field $\mathbf{u}(\mathbf{X}, t)$ and the crack phase-field $\phi(\mathbf{X}, t)$

$$\mathbf{u} : \begin{cases} \Omega \times \mathcal{T} \to \mathbb{R}^{\delta}, \\ (\mathbf{X}, t) \ \mapsto \mathbf{u}(\mathbf{X}, t), \end{cases} \qquad \text{and} \qquad \phi : \begin{cases} \Omega \times \mathcal{T} \to [0, 1], \\ (\mathbf{X}, t) \ \mapsto \phi(\mathbf{X}, t). \end{cases} \tag{1}$$

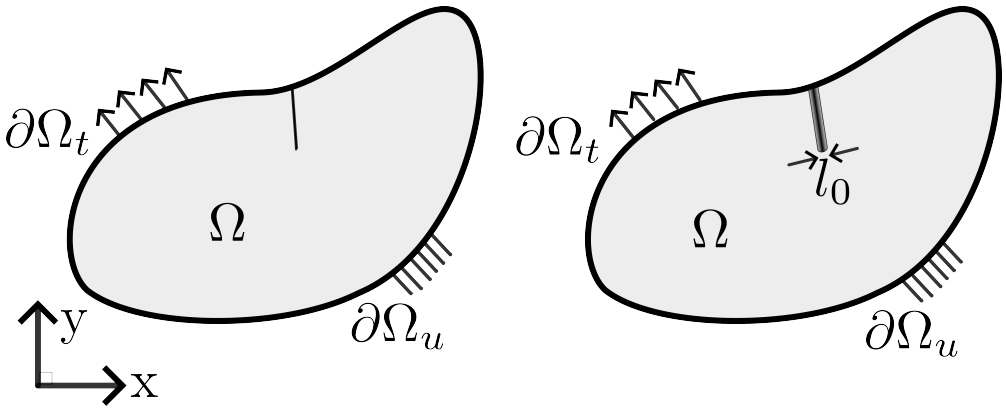

Figure 2: A 2D domain Ω with a sharp crack(left) and diffused crack(right)

The crack phase-field $\phi(\mathbf{X}, t)$ is a smeared representation of the sharp crack geometry within the volume of the body where $\phi(\mathbf{X}, t) = 0$ represents a fully intact material while $\phi(\mathbf{X}, t) = 1$ represents a fully damaged material. Fig. 2 shows a 2D domain with a sharp and diffused representation of a crack. The infinitesimal strain tensor is used to describe the kinematics of the body which is given as:

$$\boldsymbol{\varepsilon} = \frac{1}{2} \left(\nabla \mathbf{u} + \nabla \mathbf{u}^T \right). \tag{2}$$

2.1. Macroscopic and microscopic balance laws using the principle of virtual power

The governing coupled equations of the damage evolution and linear momentum balance can be derived by invoking the principle of virtual power [20]. Let $\dot{\mathbf{u}}$, $\nabla\dot{\mathbf{u}}$, $\dot{\phi}$, $\nabla\dot{\phi}$ be the kinematical descriptors. The macroscopic system is characterized by traction $\mathbf{t}(\mathbf{n})$, body force $\mathbf{b}$ which expends power over velocity $\dot{\mathbf{u}}$ and Cauchy stress tensor $\boldsymbol{\sigma}$ which expends power over displacement gradient rate $\nabla\dot{\mathbf{u}}$. The microscopic system is characterized by microscopic traction $\chi(\mathbf{n})$, scalar microscopic stress κ which expends power on the damage rate $\dot{\phi}$ and vector microscopic stress $\boldsymbol{\zeta}$ which expend power over the damage gradient rate $\nabla\dot{\phi}$. The external and internal power, $\mathcal{W}^{ext}(\mathcal{P})$ and $\mathcal{W}^{int}(\mathcal{P})$, respectively, of an arbitrary subdomain $\mathcal{P} \subset \Omega$ with boundary $\partial\mathcal{P}$ is given as:

$$\mathcal{W}_{ext}(\mathcal{P}) = \int_{\partial\mathcal{P}} \left(\mathbf{t}(\mathbf{n}) \cdot \dot{\mathbf{u}} + \chi(\mathbf{n}) \cdot \dot{\phi} \right) d(\partial\mathcal{P}) + \int_{\mathcal{P}} \mathbf{b} \cdot \dot{\mathbf{u}} \, d\mathcal{P}, \tag{3a}$$

$$\mathcal{W}_{int}(\mathcal{P}) = \int_{\mathcal{P}} \left(\boldsymbol{\sigma} : \nabla\dot{\mathbf{u}} + \boldsymbol{\zeta} \cdot \nabla\dot{\phi} + \kappa\dot{\phi} \right) d\mathcal{P}. \tag{3b}$$

Let the set $\mathcal{V} = \left(\tilde{u}, \tilde{\phi}\right)$ consist of the virtual displacement and damage fields. The principle of virtual power can thus be expressed as:

$$\int_{\partial\mathscr{P}} \left(\mathbf{t}(\mathbf{n}) \cdot \tilde{u} + \chi(\mathbf{n}) \cdot \tilde{\phi}\right) d(\partial\mathscr{P}) + \int_{\mathscr{P}} \mathbf{b} \cdot \tilde{u}\, d\mathscr{P} = \int_{\mathscr{P}} \left(\boldsymbol{\sigma} : \nabla\tilde{u} + \boldsymbol{\zeta} \cdot \nabla\tilde{\phi} + \kappa\tilde{\phi}\right) d\mathscr{P}. \tag{4}$$

Motivated by the variational approach to fracture [8, 19], the free energy density function $\hat{\psi}$ is chosen as:

$$\hat{\psi}(\phi, \nabla\phi, \boldsymbol{\varepsilon}) = \mathfrak{g}(\phi)\hat{\psi}_+^{elas}(\boldsymbol{\varepsilon}) + \hat{\psi}_-^{elas}(\boldsymbol{\varepsilon}) + \hat{\psi}^{frac}(\phi, \nabla\phi). \tag{5}$$

where $\mathfrak{g}(\phi)$ is the so called degradation function. Several options such as quadratic, cubic, linear etc. exist for choosing the degradation function [29]. In this work, a quadratic degradation function is chosen. Thus, $\mathfrak{g}(\phi) = (1-\phi)^2$. Using the spectral decomposition of the strain tensor $\boldsymbol{\varepsilon} = \sum_{i=1}^{3} \varepsilon_i \mathbf{n}_i \otimes \mathbf{n}_i$, $\hat{\psi}_+^{elas}(\boldsymbol{\varepsilon})$ and $\hat{\psi}_-^{elas}(\boldsymbol{\varepsilon})$ can be expressed as: [37],

$$\hat{\psi}^{elas}(\boldsymbol{\varepsilon})_\pm = \frac{\lambda}{2}\langle\varepsilon_1 + \varepsilon_2 + \varepsilon_3\rangle_\pm + \mu\left(\langle\varepsilon_1\rangle_\pm^2 + \langle\varepsilon_2\rangle_\pm^2 + \langle\varepsilon_3\rangle_\pm^2\right), \tag{6}$$

where λ and ν are the Lamé's parameters. $\langle x\rangle_\pm$ are the ramp functions defined as $\langle x\rangle_+ = \frac{|x|+x}{2}$ and $\langle x\rangle_- = \frac{|x|-x}{2}$. The fracture surface free energy density $\hat{\psi}^{frac}$, with G_c as the critical energy release rate and l_0 as the regularisation length is taken as the AT2 model [37]

$$\hat{\psi}^{frac} = \frac{G_c}{2l_0}\left(\phi^2 + l_0^2\nabla\phi \cdot \nabla\phi\right). \tag{7}$$

Taking arbitrary values of the virtual fields $\mathcal{V}$, in Eq. 4, using the first and second laws of thermodynamics, the free energy density function in Eq. 5 and incorporating crack irreversibility through a history function [37] ($\mathscr{H}$), the macroforce and microforce balance laws and the associated boundary conditions can be expressed as [20, 16]

$$\nabla \cdot \boldsymbol{\sigma} + \mathbf{b} = \mathbf{0} \quad \text{in} \quad \Omega, \tag{8a}$$

$$\boldsymbol{\sigma} \cdot \mathbf{n} = \bar{\mathbf{t}} \quad \text{on} \quad \partial\Omega_t, \tag{8b}$$

$$\mathbf{u} = \bar{\mathbf{u}} \quad \text{on} \quad \partial\Omega_u, \tag{8c}$$

$$\frac{G_c}{l_0}\left(\phi - l_0^2\Delta\phi\right) = 2\left(1-\phi\right)\mathscr{H} \quad \text{in} \quad \Omega, \tag{8d}$$

$$\nabla\phi \cdot \mathbf{n} = 0 \quad \text{on} \quad \partial\Omega, \tag{8e}$$

where the cauchy stress tensor ($\boldsymbol{\sigma}$) and the history function ($\mathscr{H}$) are defined as:

$$\boldsymbol{\sigma} = (1-\phi)^2\frac{\partial\hat{\psi}_+^{elas}(\boldsymbol{\varepsilon})}{\partial\boldsymbol{\varepsilon}} + \frac{\partial\hat{\psi}_-^{elas}(\boldsymbol{\varepsilon})}{\partial\boldsymbol{\varepsilon}}, \tag{9a}$$

$$\mathscr{H}(\hat{\psi}_+^{elas}(\boldsymbol{\varepsilon})) = \max_{s\in[0,\tau]} \hat{\psi}_+^{elas}(\boldsymbol{\varepsilon}(s)). \tag{9b}$$

3. Virtual element method formulation

Consider a 2D domain as shown in Fig. 2 discretised by a set $\mathcal{E}_h$, consisting of N non-overlapping polygons. For any element $E \in \mathcal{E}_h$, with its boundary ∂E, let $\mathbf{x}_E = (x_c, y_c)$, h_E, $|E|$ respectively denote the centroid, diameter and area of the element E. The polygon has N_v number of vertices and edges with any vertex and edge denoted by V_i and e_i, respectively, with $i = 1, 2, 3, ..., N_v$. Any edge e_i connects the vertices V_i and V_{i+1}. Note that e_{N_v} connects vertices V_1 and V_{N_v}. Let $\mathrm{P}_k(E)$ denote the space of complete polynomials of degree k over

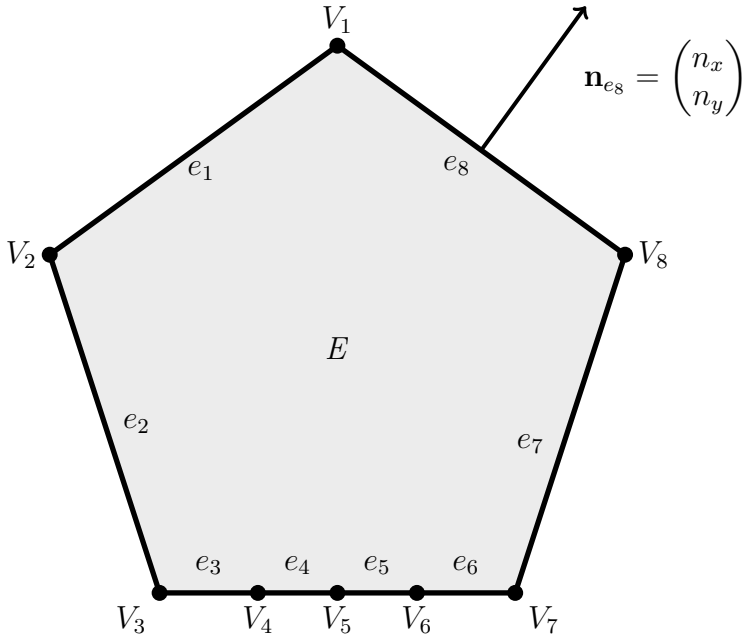

Figure 3: An 8-noded polygon with hanging nodes V_4, V_5, V_6 on the bottom edge.

the element E. A suitable choice for the basis of $\mathrm{P}_k(E)$ is $\mathrm{M}_k(E)$, which consists of scaled monomials of degree less than or equal to k. In two dimensions, for the case of $k = 1$ with one degree of freedom per node, $\mathrm{M}_1(E)$ can be expressed as:

$$\mathrm{M}_1(E) = \{m_1, m_2, m_3\} = \big\{1, \xi, \eta\big\}, \tag{10}$$

where ξ and η are the scaled monomials defined as:

$$\xi = \frac{x - x_c}{h_E}, \tag{11a}$$

$$\eta = \frac{y - y_c}{h_E}. \tag{11b}$$

For the case of 2D elastostatics for $k = 1$, where there are two degrees of freedom per node, the polynomial space $\mathbf{M}_1(E) \equiv [\mathrm{M}_1(E)]^2$ has a dimension of 6, which can be expressed

as:

$$\mathbf{M}_1(E) = \{\mathbf{m}_1, \mathbf{m}_2, \mathbf{m}_3, \mathbf{m}_4, \mathbf{m}_5, \mathbf{m}_6\} = \left[\begin{pmatrix}1\\0\end{pmatrix}, \begin{pmatrix}0\\1\end{pmatrix}, \begin{pmatrix}-\eta\\\xi\end{pmatrix}, \begin{pmatrix}\eta\\\xi\end{pmatrix}, \begin{pmatrix}\xi\\0\end{pmatrix}, \begin{pmatrix}0\\\eta\end{pmatrix}\right],$$

where the choice of first three vectors $\mathbf{m}_1, \mathbf{m}_2, \mathbf{m}_3$ is made to ensure that the rigid body modes can be captured. These mathematical preliminaries will be used in the derivation of the elemental stiffness matrix of any general polygonal shape for the discretised equations of damage evolution and equilibrium in the subsequent sections.

3.1. Virtual element spaces of the damage and elasticity subproblem

The weak form of the governing differential equations for the damage subproblem (Eq. 8d, 8e) and the linear momentum balance (Eq. 8a, 8b, 8c) can be stated as:

$$\begin{cases} \text{Find } \phi \in \mathcal{V}_\phi = H_0^1(\Omega) \text{ and } \mathbf{u} \in \mathcal{V}_\mathbf{u} = [H_0^1(\Omega)]^2 \text{ such that:} \\ \mathcal{B}_\phi(\phi, v_\phi) = L_\phi(v_\phi), \quad \forall v_\phi \in \mathcal{V}_\phi, \\ \mathcal{B}_\mathbf{u}(\mathbf{u}, \mathbf{v}_\mathbf{u}) = L_\mathbf{u}(\mathbf{v}_\mathbf{u}), \quad \forall \mathbf{v}_\mathbf{u} \in \mathcal{V}_\mathbf{u}, \end{cases} \tag{12}$$

where, $H_0^1(\Omega)$ indicates the first order Sobolev space. The bilinear forms $\mathcal{B}_\phi(\phi, v_\phi)$, $\mathcal{B}_\mathbf{u}(\mathbf{u}, \mathbf{v}_\mathbf{u})$ and the linear form $L(v_\phi)$, $L(\mathbf{v}_\mathbf{u})$ are given as:

$$\mathcal{B}_\phi(\phi, v_\phi) = \int_\Omega (G_c l_0) \nabla\phi \cdot \nabla v_\phi \, d\Omega + \int_\Omega \left(\frac{G_c}{l_0} + 2\mathscr{H}\right) \phi v_\phi \, d\Omega, \tag{13a}$$

$$\mathcal{B}_\mathbf{u}(\mathbf{u}, \mathbf{v}_\mathbf{u}) = \int_\Omega \boldsymbol{\sigma}(\mathbf{u}) : \boldsymbol{\epsilon}(\mathbf{v}_\mathbf{u}) \, d\Omega, \tag{13b}$$

$$L_\phi(v_\phi) = \int_\Omega 2\mathscr{H} v_\phi \, d\Omega, \tag{13c}$$

$$L_\mathbf{u}(\mathbf{v}_\mathbf{u}) = \int_{\partial\Omega} \mathbf{v}_\mathbf{u} \cdot \bar{\mathbf{t}} \, d(\partial\Omega_t). \tag{13d}$$

Let $\mathcal{V}_{\phi,h}$ and $\mathcal{V}_{\mathbf{u},h}$ denote the finite dimensional subspaces of $\mathcal{V}_\phi$ and $\mathcal{V}_\mathbf{u}$ repectively. These spaces are constructed by the assembly of $\mathcal{V}_{\phi,h}(E)$ and $\mathcal{V}_{\mathbf{u},h}(E)$ over the elements $E \in \mathrm{P}_h$. The local virtual element spaces, $\mathcal{V}_{\phi,h}(E)$ and $\mathcal{V}_{\mathbf{u},h}(E)$ over an element E, are defined as:

$$\begin{aligned} \mathcal{V}_{\phi,h}(E) \coloneqq \big\{ & v_{\phi,h} : v_{\phi,h} \in H^1(E), \quad \Delta v_{\phi,h} = 0, \quad v_{\phi,h}|_e \in \mathrm{P}_1(e), \\ & \forall e \in \partial E, \quad v_{\phi,h}|_{\partial E} \in C^0(\partial E) \big\}, \end{aligned} \tag{14a}$$

$$\begin{aligned} \mathcal{V}_{\mathbf{u},h}(E) \coloneqq \big\{ & \mathbf{v}_{\mathbf{u},h} : \mathbf{v}_{\mathbf{u},h} \in [H^1(E)]^2, \quad \Delta\mathbf{v}_{\mathbf{u},h} \in [\mathrm{P}_1(e)]^2, \\ & \mathbf{v}_{\mathbf{u},h}|_e \in [\mathrm{P}_1(e)]^2 \quad \forall e \in \partial E, \quad \mathbf{v}_{\mathbf{u},h}|_{\partial E} \in C^0(\partial E) \big\}. \end{aligned} \tag{14b}$$

For $\mathcal{V}_{\phi,h}(E)$ and $\mathcal{V}_{\mathbf{u},h}(E)$ defined as in Eq. (14), the degrees of freedom can be chosen as the values of ϕ_h and $\mathbf{u}_h(u_h^x, u_h^y)$ at the vertices of E. Thus the dimension of $\mathcal{V}_{\phi,h}(E)$ and

$\mathcal{V}_{\mathbf{u},h}(E)$ is N_v and $2N_v$ respectively. The global virtual element space $\mathcal{V}_{\phi,h}$ and $\mathcal{V}_{\mathbf{u},h}$ can now be defined as:

$$\mathcal{V}_{\phi,h} \coloneqq \left\{ v_{\phi,h} : v_{\phi,h} \in H_0^1(\Omega), \quad v_{\phi,h}|_e \in \mathcal{V}_{\phi,h}(E) \quad \forall E \in \mathcal{E}_h \right\}, \tag{15a}$$

$$\mathcal{V}_{\mathbf{u},h} \coloneqq \left\{ \mathbf{v}_{\mathbf{u},h} : \mathbf{v}_{\mathbf{u},h} \in [H_0^1(\Omega)]^2, \quad \mathbf{v}_{\mathbf{u},h}|_e \in \mathcal{V}_{\mathbf{u},h}(E) \quad \forall E \in \mathcal{E}_h \right\}. \tag{15b}$$

3.2. Computation of the projection operator

A crucial ingredient of the virtual element method is the construction of the projection operator that approximates the bilinear form Eq.(13a) and Eq.(13b). The finite-dimensional bilinear form of the damage and displacement subproblem over an element E can be expressed using the virtual element spaces Eq.(14) as:

$$\mathcal{B}_{\phi,h,E}(\phi_h, v_{\phi,h}) = \mathcal{B}^d_{\phi,h,E}(\phi_h, v_{\phi,h}) + \mathcal{B}^r_{\phi,h,E}(\phi_h, v_{\phi,h}), \tag{16a}$$

$$\mathcal{B}_{\mathbf{u},h,E}(\mathbf{u}_h, \mathbf{v}_{\mathbf{u},h}) = \int_E \boldsymbol{\sigma}(\mathbf{u}_h) : \boldsymbol{\epsilon}(\mathbf{v}_{\mathbf{u},h})\, dE, \tag{16b}$$

where, $\mathcal{B}^d_{\phi,h}(\phi_h, v_{\phi,h})$ and $\mathcal{B}^r_{\phi,h}(\phi_h, v_{\phi,h})$, respectively, denote the diffusion and reaction terms of the bilinear form Eq. (16a). These are given as:

$$\mathcal{B}^d_{\phi,h,E}(\phi_h, v_{\phi,h}) = (G_c l_0) \int_E \nabla\phi_h \cdot \nabla v_{\phi,h}\, dE, \tag{17a}$$

$$\mathcal{B}^r_{\phi,h,E}(\phi_h, v_{\phi,h}) = \left(\frac{G_c}{l_0} + 2\mathscr{H} \right) \int_E \phi_h v_{\phi,h}\, dE. \tag{17b}$$

Let $\Pi^\nabla_\phi : \mathcal{V}_{\phi,h}(E) \to \mathrm{M}_1(E)$, $\Pi^0_\phi : \mathcal{V}_{\phi,h}(E) \to \mathrm{M}_1(E)$ and $\Pi^\nabla_{\mathbf{u}} : \mathcal{V}_{\mathbf{u},h}(E) \to \mathbf{M}_1(E)$ denote the projection operators corresponding to the bilinear forms $\mathcal{B}^d_{\phi,h,E}$, $\mathcal{B}^r_{\phi,h,E}$ and $\mathcal{B}_{\mathbf{u},h,E}(\mathbf{u}_h, \mathbf{v}_{\mathbf{u},h})$, respectively. These can be defined by making use of the orthogonality conditions [58].

Let ψ_i denote the canonical basis of $\mathcal{V}_{\phi,h}(E)$, i.e., $\psi_i(V_j) = \delta_{ij}$, where δ_{ij} is the Kronecker delta symbol and $i, j = 1, 2, \cdots, N_v$. Let $\boldsymbol{\Psi}_i = \{\psi_i \ 0\}^T$ and $\boldsymbol{\Psi}_{N^v+i} = \{0 \ \psi_i\}^T$ denote the $2N_v$ vectorial canonical basis functions for the displacement subproblem.

Thus, for each basis $\psi_i \in \mathcal{V}_{\phi,h}(E)$, $\boldsymbol{\Psi}_{\mathtt{i}} \in \mathcal{V}_{\mathbf{u},h}(E)$, $\forall m_\alpha \in \mathrm{M}_1(E)$, $\forall \mathbf{m}_{\bar{\alpha}} \in \mathbf{M}_1(E)$, where $i = 1, \cdots, N_v$, $\mathtt{i} = 1, \cdots, 2N_v$, $\alpha = 1, 2, 3$ and $\bar{\alpha} = 1, 2, \cdots, 6$, the orthogonality conditions can be stated as:

$$\mathcal{B}^d_{\phi,h,E}\left(m_\alpha, \left(\Pi^\nabla_\phi \psi_i - \psi_i\right)\right) = 0, \tag{18a}$$

$$\mathcal{B}^r_{\phi,h,E}\left(m_\alpha, \left(\Pi^0_\phi \psi_i - \psi_i\right)\right) = 0, \tag{18b}$$

$$\mathcal{B}_{\mathbf{u},h,E}\left(\mathbf{m}_{\bar{\alpha}}, \left(\Pi^\nabla_{\mathbf{u}} \boldsymbol{\Psi}_{\mathtt{i}} - \boldsymbol{\Psi}_{\mathtt{i}}\right)\right) = 0. \tag{18c}$$

For $\alpha = 1$ and $\bar{\alpha} = 1, 2, 3$ Eq.(18a) and Eq.(18c) leads to a trivial solution. Thus Eq.(18) are supplemented with the following additional equations:

$$P_0\big(m_\alpha, \left(\Pi^\nabla_\phi \psi_i - \psi_i\right)\big) = 0 \quad (\alpha = 1), \tag{19a}$$

$$\mathbf{P}_0\big(\mathbf{m}_{\bar{\alpha}}, \left(\Pi^\nabla_{\mathbf{u}} \boldsymbol{\Psi}_{\mathtt{i}} - \boldsymbol{\Psi}_{\mathtt{i}}\right)\big) = 0 \quad (\bar{\alpha} = 1, 2, 3). \tag{19b}$$

where, $P_0(a,b)$ and $\mathbf{P}_0(\mathbf{a},\mathbf{b})$ are defined as:

$$P_0(a,b) = \frac{1}{N_v}\sum_{j=1}^{N_v} a(x_j)b(x_j), \tag{20a}$$

$$\mathbf{P}_0(\mathbf{a},\mathbf{b}) = \frac{1}{N_v}\sum_{j=1}^{N_v} \mathbf{a}(\mathbf{x}_j)\cdot\mathbf{b}(\mathbf{x}_j). \tag{20b}$$

If s_i^β and π_i^β denote the coefficients of $\Pi_\phi^\nabla\psi_i$ and $\Pi_{\mathbf{u}}^\nabla\mathbf{\Psi}_{\mathtt{i}}$ with respect to the basis $\mathrm{M}_1(E)$ and $\mathbf{M}_1(E)$ respectively (where $i = 1,...,N_v$ and $\mathtt{i} = 1,\cdots,2N_v$) then

$$\Pi_\phi^\nabla\psi_i = \sum_{\beta=1}^{3} s_i^\beta m_\beta, \tag{21a}$$

$$\Pi_{\mathbf{u}}^\nabla\mathbf{\Psi}_{\mathtt{i}} = \sum_{\beta=1}^{6} \pi_i^\beta \mathbf{m}_\beta. \tag{21b}$$

Substituting Eq.(21) in Eq.(18a),(18c), using Eq.(19), making use of the linear momentum balance and the divergence theorem to convert the volume integral to boundary integral, the matrix representation of Π_ϕ^∇ and $\Pi_{\mathbf{u}}^\nabla$ with respect to the polynomial bases $\mathrm{M}_1(E)$ and $\mathbf{M}_1(E)$ can be obtained as:

$$\Pi_\phi^\nabla = G^{-1}B, \tag{22a}$$

$$\Pi_{\mathbf{u}}^\nabla = \mathbf{G}^{-1}\mathbf{B}. \tag{22b}$$

The matrices G and B can be expressed as

$$G_{\alpha\beta} = \begin{cases} \dfrac{1}{N_v}\displaystyle\sum_{j=1}^{N_v} m_\beta(V_j), & (\alpha = 1 \quad \& \quad \beta = 1,2,3), \\ \displaystyle\int_E \nabla m_\alpha\cdot\nabla m_\beta\, dE, & (\text{otherwise}), \end{cases} \tag{23a}$$

$$B_{\alpha i} = \begin{cases} \dfrac{1}{N_v}\displaystyle\sum_{j=1}^{N_v} \psi_i(V_j), & (\alpha = 1 \quad \& \quad i = 1,2,\cdots,N_v), \\ \displaystyle\int_E \nabla m_\alpha\cdot\nabla \psi_i\, dE, & (\text{otherwise}). \end{cases} \tag{23b}$$

Similarly, the matrices $\mathbf{G}$ and $\mathbf{B}$ can be expressed as:

$$\mathbf{G}_{\bar{\alpha}\bar{\beta}} = \begin{cases} \dfrac{1}{N_v}\displaystyle\sum_{j=1}^{N_v} \mathbf{m}_{\bar{\alpha}}(\mathbf{x}_j).\mathbf{m}_{\bar{\beta}}(\mathbf{x}_j), & (\bar{\alpha}=1,2,3), \\ \displaystyle\sum_{j=1}^{N_v} \mathbf{m}_{\bar{\beta}}(\mathbf{x}_j)\cdot\boldsymbol{\sigma}(\mathbf{m}_{\bar{\alpha}})\left(\frac{|e_{j-1}|}{2}\mathbf{n}_{e_{j-1}}+\frac{|e_j|}{2}\mathbf{n}_{e_j}\right) & (\text{otherwise}), \end{cases} \tag{24a}$$

$$\mathbf{B}_{\bar{\alpha}\mathtt{i}} = \begin{cases} \dfrac{1}{N_v}\displaystyle\sum_{j=1}^{N_v} \mathbf{m}_{\bar{\alpha}}(\mathbf{x}_j).\boldsymbol{\Psi}_{\mathtt{i}}(\mathbf{x}_j), & (\bar{\alpha}=1,2,3), \\ \displaystyle\sum_{j=1}^{N_v} \boldsymbol{\Psi}_{\mathtt{i}}(\mathbf{x}_j)\cdot\boldsymbol{\sigma}(\mathbf{m}_{\bar{\alpha}})\left(\frac{|e_{j-1}|}{2}\mathbf{n}_{e_{j-1}}+\frac{|e_j|}{2}\mathbf{n}_{e_j}\right) & (\text{otherwise}). \end{cases} \tag{24b}$$

In Eq.(24a) and (24b), $\mathbf{n}_{e_j}$ represents the outward normal vector to the edge connecting the vertices j and $j+1$ as shown in Fig. 3. For $j=N_v$, this would be the edge connecting the vertices $j=1$ and $j=N_v$. Furthermore, the Cauchy stress tensor in Eq.(24a) and (24b) is the coupled through the phase-field variable (ϕ) as:

$$\boldsymbol{\sigma}(\mathbf{m}_{\bar{\alpha}}) = (1-\phi)^2\mathbf{C}_0\boldsymbol{\epsilon}(\mathbf{m}_{\bar{\alpha}}), \tag{25}$$

where, $\mathbf{C}_0$ is the undegraded elasticity constitutive matrix. Choosing ϕ as the nodal values of the phase-field in Eq.(24a) and (24b) leads to an anisotropic elastic stiffness matrix. To avoid this, we define the Cauchy stress tensor as:

$$\boldsymbol{\sigma}(\mathbf{m}_{\bar{\alpha}}) = (1-\bar{\phi})^2\mathbf{C}_0\boldsymbol{\epsilon}(\mathbf{m}_{\bar{\alpha}}), \tag{26}$$

where, we introduce the nodal average phase-field $\bar{\phi}$ defined as:

$$\bar{\phi} = \sum_{j=1}^{N_v}\frac{\phi_j}{N_v}. \tag{27}$$

The projection operator Π^0_ϕ in Eq.(18b) is the L^2 projection operator onto the polynomial space $\mathrm{M}_1(E)$. It can be easily shown that for projection onto the space $\mathrm{M}_1(E)$, the L^2 projection operator is equal to the projection operator for the diffusion term. Thus,

$$\Pi^0_\phi = \Pi^\nabla_\phi. \tag{28}$$

If $\boldsymbol{\Pi}^\nabla_\phi$ and $\boldsymbol{\Pi}^\nabla_{\mathbf{u}}$ represent the components of Π^∇_ϕ and $\Pi^\nabla_{\mathbf{u}}$ with respect to the canonical bases ψ_i and $\boldsymbol{\Psi}_{\mathtt{i}}$, respectively. Then these can be expressed as:

$$\boldsymbol{\Pi}^\nabla_\phi = D\Pi^\nabla_\phi, \tag{29a}$$

$$\boldsymbol{\Pi}^\nabla_{\mathbf{u}} = \mathbf{D}\Pi^\nabla_{\mathbf{u}}, \tag{29b}$$

where, the matrices D and $\mathbf{D}$ are given as:

$$D_{i\alpha} = \mathtt{dof}_i(m_\alpha), \tag{30a}$$

$$\mathbf{D}_{\mathtt{i}\bar{\alpha}} = \mathtt{dof}_{\mathtt{i}}(\mathbf{m}_{\bar{\alpha}}), \tag{30b}$$

where, the $\mathtt{dof}_k(\cdot)$ operator gives the value of any input at the k^{th} degree of freedom.

3.3. Computation of the elemental stiffness matrices

The elemental stiffness matrix for the damage subproblem can be computed as:

$$\begin{aligned}\mathbf{K}_{\phi,E} &= \mathcal{B}_{\phi,h,E}(\psi_i,\psi_j)\\ &= \mathcal{B}^d_{\phi,h,E}(\psi_i+\Pi^\nabla_\phi\psi_i-\Pi^\nabla_\phi\psi_i,\psi_j+\Pi^\nabla_\phi\psi_j-\Pi^\nabla_\phi\psi_j)+\mathcal{B}^r_{\phi,h,E}(\Pi^0_\phi\psi_i,\Pi^0_\phi\psi_j)\\ &= \underbrace{(\Pi^\nabla_\phi)^T\left((G_cl_0)\bar{G}+\left(\frac{G_c}{l_0}+2\mathscr{H}\right)H\right)(\Pi^\nabla_\phi)}_{\text{Consistency term}}+\underbrace{(G_cl_0)(\mathbf{I}-\mathbf{\Pi}^\nabla_\phi)^T(\mathbf{I}-\mathbf{\Pi}^\nabla_\phi)}_{\text{Stability term}},\end{aligned}\tag{31}$$

where the matrix $\bar{G}$ is the G matrix in Eq.(23a) with the entries with the first row set to zeros and the matrix H is defined as:

$$H=\int_E m_\alpha m_\beta\,dE.\tag{32}$$

Similarly, the elemental stiffness matrix for the displacement subproblem can be computed as:

$$\begin{aligned}\mathbf{K}_{\mathbf{u},E} &= \mathcal{B}_{\mathbf{u},h,E}\left(\mathbf{\Psi}_\mathtt{i},\mathbf{\Psi}_\mathtt{j}\right)\\ &= \mathcal{B}_{\mathbf{u},h,E}\left(\Pi^\nabla_\mathbf{u}\mathbf{\Psi}_\mathtt{i},\Pi^\nabla_\mathbf{u}\mathbf{\Psi}_\mathtt{j}\right)+\mathcal{B}_{\mathbf{u},h,E}\left(\left(\mathbf{I}-\mathbf{\Pi}^\nabla_\mathbf{u}\right)\mathbf{\Psi}_\mathtt{i},\left(\mathbf{I}-\mathbf{\Pi}^\nabla_\mathbf{u}\right)\mathbf{\Psi}_\mathtt{j}\right)\\ &= \underbrace{(\Pi^\nabla_\mathbf{u})^T\bar{\mathbf{G}}(\Pi^\nabla_\mathbf{u})}_{\text{Consistency term}}+\underbrace{(\mathbf{I}-\mathbf{\Pi}^\nabla_\mathbf{u})^T\mathbf{S}^d_E(\mathbf{I}-\mathbf{\Pi}^\nabla_\mathbf{u})}_{\text{Stability term}},\end{aligned}\tag{33}$$

where the matrix $\bar{\mathbf{G}}$ is the $\mathbf{G}$ matrix in Eq.(24a) with the entries of first three rows set to zero. We further define the diagonal matrix $\mathbf{S}^d_E$ to introduce an additional dependence on the phase-field variable through $\bar{\phi}$ as:

$$(\mathbf{S}^d_E)_{\mathtt{ii}}=max\left((1-\bar{\phi})^2tr(\mathbf{C}_0)/3,(\mathbf{K}^c_{\mathbf{u},E})_{\mathtt{ii}}\right),\tag{34}$$

where, $tr(\cdot)$ is the trace operator and $\mathbf{K}^c_{\mathbf{u},E}$ denotes the consistency matrix of the displacement subproblem.

3.4. Computation of the History and load term

The history energy function of an element $\mathscr{H}(E,t)$, which is a measure of the maximum stored energy density, is calculated based on the average strain measure over an element $\boldsymbol{\varepsilon}_{avg}(E)$, which can be expressed as,

$$\boldsymbol{\varepsilon}_{avg}(E)=\frac{1}{E}\int_E\boldsymbol{\varepsilon}\,dE=\frac{\nabla\left(\mathbf{\Pi}^\nabla_\mathbf{u}\mathbf{u}\right)+\nabla\left(\mathbf{\Pi}^\nabla_\mathbf{u}\mathbf{u}^T\right)}{2E}.\tag{35}$$

where the final form is derived by applying the divergence theorem to the strain-displacement relation in Eq. (2). Since $\mathbf{\Pi}^\nabla_\mathbf{u}\in[\mathrm{P}_1(e)]^2$, $\boldsymbol{\varepsilon}_{avg}$ is constant within an element. Thus, $\mathscr{H}(E,t)$ can be evaluated as:

$$\mathscr{H}(E,t)=\max_{s\in[0,t]}\hat{\psi}^{elas}_+(\boldsymbol{\varepsilon}_{avg}(E),s).\tag{36}$$

The load term $L_{\phi,h}(\phi)$ can be calculated by making use of the L^2 projection operator Π^0_ϕ. So, we have from Eq. (13c,28)

$$L_{\phi,h}(\psi_i) = 2\mathscr{H} \int_E \psi_i \, dE = 2\mathscr{H} \int_E \Pi^\nabla_\phi \psi_i \, dE = 2\mathscr{H} (\Pi^\nabla_\phi)^T H(:,1), \tag{37}$$

where, $H(:,1)$ represents the first column of the matrix H. The load term for the displacement subproblem can similarly be obtained. Finally, the global stiffness matrices for the damage and displacement subproblems can be constructed by performing a standard assembly operation on the elemental stiffness matrices, $\mathbf{K}_{\phi,E}$ and $\mathbf{K}_{\mathbf{u},E}$, respectively.

4. Numerical simulations

We now present numerical simulations to evaluate the virtual element method's (VEM) efficacy in modeling brittle crack propagation using the phase-field method. In Section 4.1, we demonstrate that a VEM mesh can significantly reduce the degrees of freedom without compromising accuracy. Additionally, we illustrate that the use of too many hanging nodes can lead to inaccurate results. Next, in Section 4.2, we present guidelines for fixing the number and position of hanging nodes using the K-field loading conditions of linear elastic fracture mechanics (LEFM). We apply this refinement strategy to the problem of a symmetric three-point bend test in Section 4.3, asymmetric three-point bend test in Section 4.4 and a compact tension specimen under mixed-mode I + II loading in Section 4.5. Additionally, in Section 4.5, we introduce a semi-adaptive refinement strategy framework, where virtual elements can be easily implemented in the commercial software Abaqus to solve problems where the crack path is not known *a priori*.

All numerical simulations are performed in the commercial finite element software Abaqus [17]. The element stiffness matrices, residual vector, and load vector for VEM are implemented by writing user-defined element (UEL) subroutines in Abaqus. To display the virtual elements with hanging nodes, the results are mapped to a 4-noded dummy quadrilateral element. The dummy quadrilateral element is assigned negligible stiffness using a UMAT subroutine. The simulations are performed on a Windows machine (Intel(R) Core(TM) i9-9900KF CPU @ 3.60GHz with 64 GB of RAM). The following procedure is used to generate elements with hanging nodes:

- First, the region containing elements with hanging nodes is partitioned.
- The adjoining regions are meshed with fine and coarse meshes in the Abaqus preprocessor. Nodes at the boundary between the fine and coarse mesh are marked, and the input file is generated.
- A MATLAB script is developed to take the Abaqus input file and generate elements with hanging nodes using the information about nodes present at the boundary between the fine and coarse mesh regions.

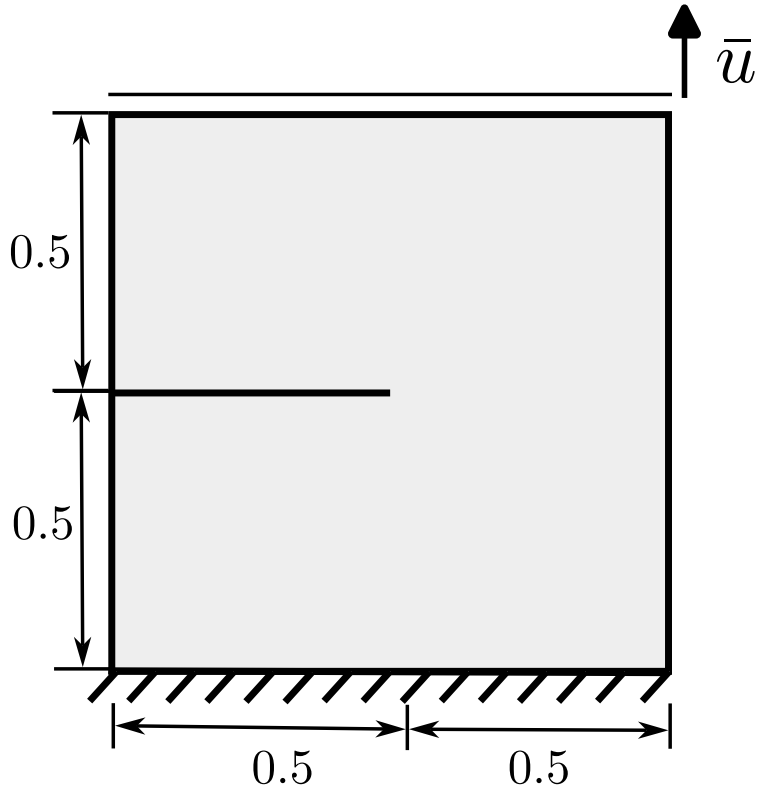

Figure 4: Schematic of the SENT specimen

4.1. Single edge notch tension test

The single edge notch test (SENT) is a common benchamark study used in phase-field fracture simulations in the litearature [1, 3, 37]. The SENT specimen consists of a square plate of dimensions $1\,mm \times 1\,mm$ with a horizontal notch of length $0.5\,mm$ placed mid-height as shown in Fig. 4. The out-of-plane thickness is considered to be $1\,mm$, and plane strain conditions are assumed. A uniform vertical displacement loading is applied at the top end, while keeping the horizontal displacement fixed and the specimen is fixed in both the horizontal and vertical directions at the bottom end. The material properties used in the simulations are taken from [37] where the Lamé's parameters are taken as $\lambda = 121150\text{N}/mm^2$ and $\mu = 80769.2\ \text{N}/mm^2$. The fracture parameters which are the critical energy release rate (G_c) and the length scale (l_0) used in phase-field fracture simulations are taken as $G_c = 2.7\,\text{N/mm}$ and $l_0 = 0.015\,\text{mm}$. The mesh size near the notch (h_0) is taken to be 0.001 mm, resulting in a l_0/h_0 ratio of 15, sufficient to resolve the phase-field near the crack. A total displacement of 0.007 mm is applied.

The simulation is performed in a domain discretised primarily with 4-noded plane strain finite and virtual elements. Fig. 5 shows the discretised SENT assembly. The 4-noded plane strain finite element is denoted as FEM CPE4 while the corresponding virtual element is denoted as VEM CPE4.

Since a virtual element discretization permits elements with any number of nodes while

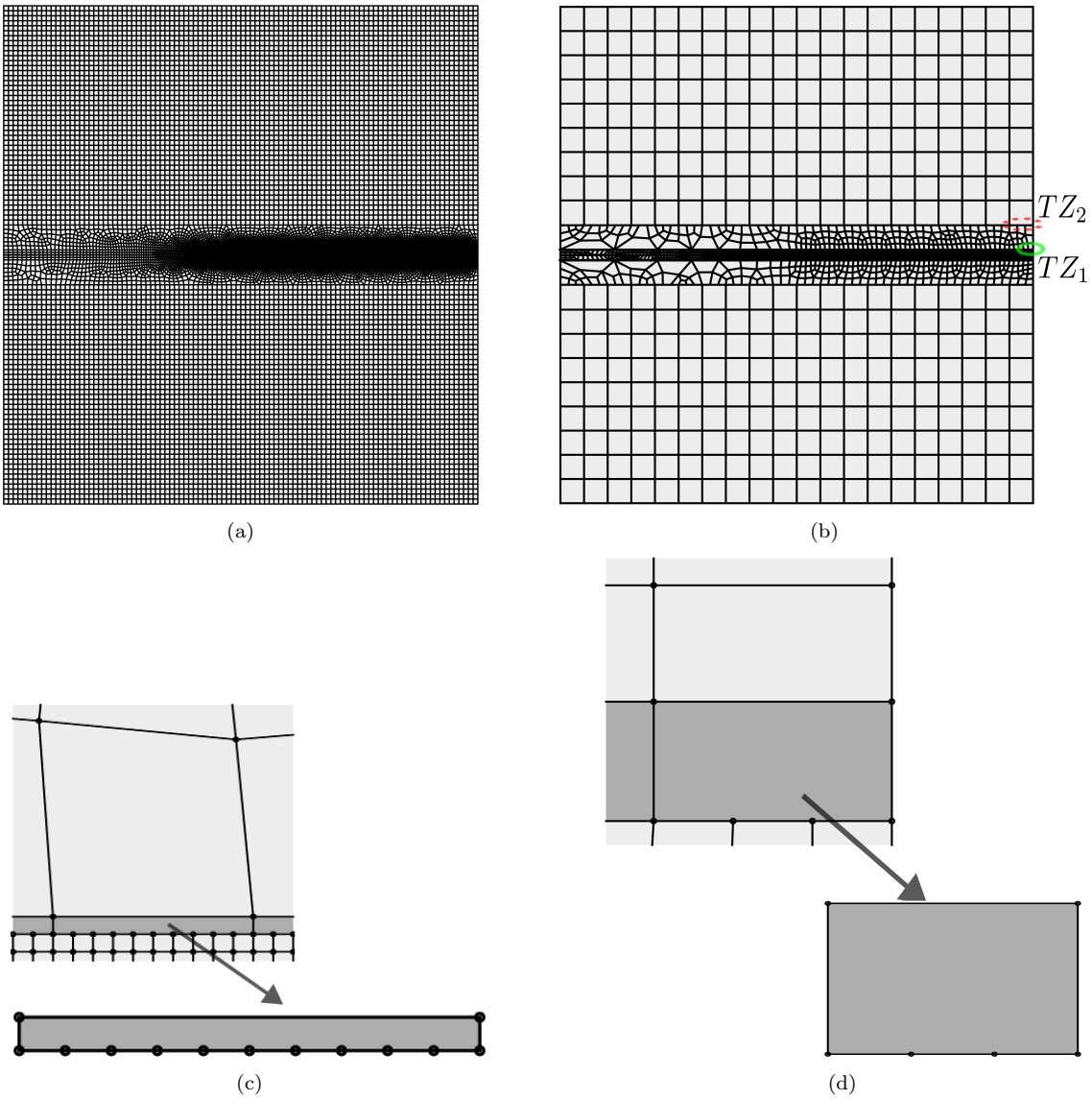

Figure 5: Discretization schemes used in the simulations (a) Domain discretised with FEM CPE4 and VEM CPE4 mesh (b) Domain discretised with VEM HN1 mesh (c) Zoomed in region of the transition zone TZ_1 highlighting the 13-noded element (d) Zoomed in region of the transition zone TZ_2 highlighting the 6-noded element

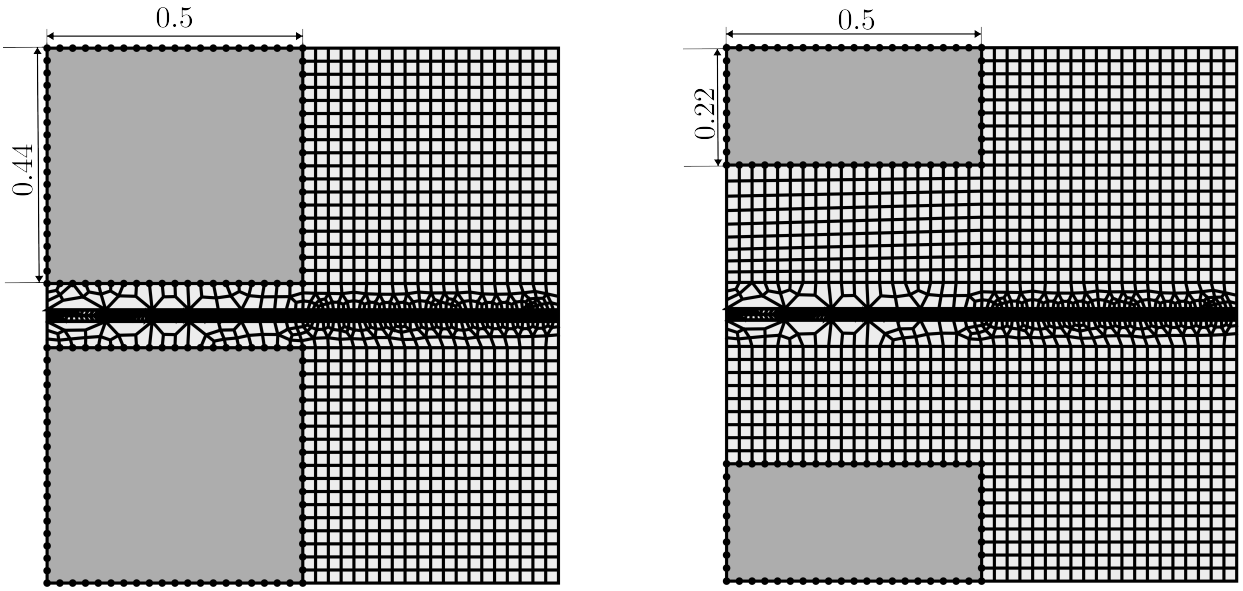

Figure 6: Meshes with a large number of hanging nodes. The dark grey region shows a single element with (a) 77 nodes (b) 58 nodes

maintaining the conformity of the primary unknowns across element boundaries, we consider the following three meshes with elements having varying number of hanging nodes,

- **VEM HN1**: In this mesh, 13-noded and 6-noded virtual elements as shown in Fig. 5c and Fig. 5d are used in the transition zones (TZ_1, TZ_2) as highlighted in Fig. 5b.
- **VEM HN2**: In this mesh, a 77-noded single element is used along with the 13-noded transition element in the transition zone TZ_1 as shown in Fig. 6a.
- **VEM HN3**: In this mesh, a 58-noded single element is used along with the 13-noded transition element in the transition zone TZ_1 as shown in Fig. 6b.

Fig. 7 shows the reaction vs displacement plots for different discretization schemes. The difference in peak reaction force between FEM CPE4 and VEM HN1 mesh is less than 2 %. An additional simulation with a VEM voronoi mesh (VEM VORO) consisting of a mixture of polygons with number of sides ranging from 4 to 9 is also done to highlight the model's capability in dealing with polygonal elements.

However, significant error accrues in the VEM HN2 mesh in the initial elastic stiffness, peak reaction force and the post-peak behaviour. For the VEM HN3 mesh, the error in these parameters reduces as compared to the VEM HN2 mesh, but the peak reaction force and the post peak displacement response is still not comparable with the VEM CPE4, FEM CPE4 and the VEM HN1 mesh. This shows the limitations of using virtual elements with a very large number of nodes in phase-field fracture simulations. Further discussion on the effect of large number of hanging nodes will be presented in Section. 4.2.

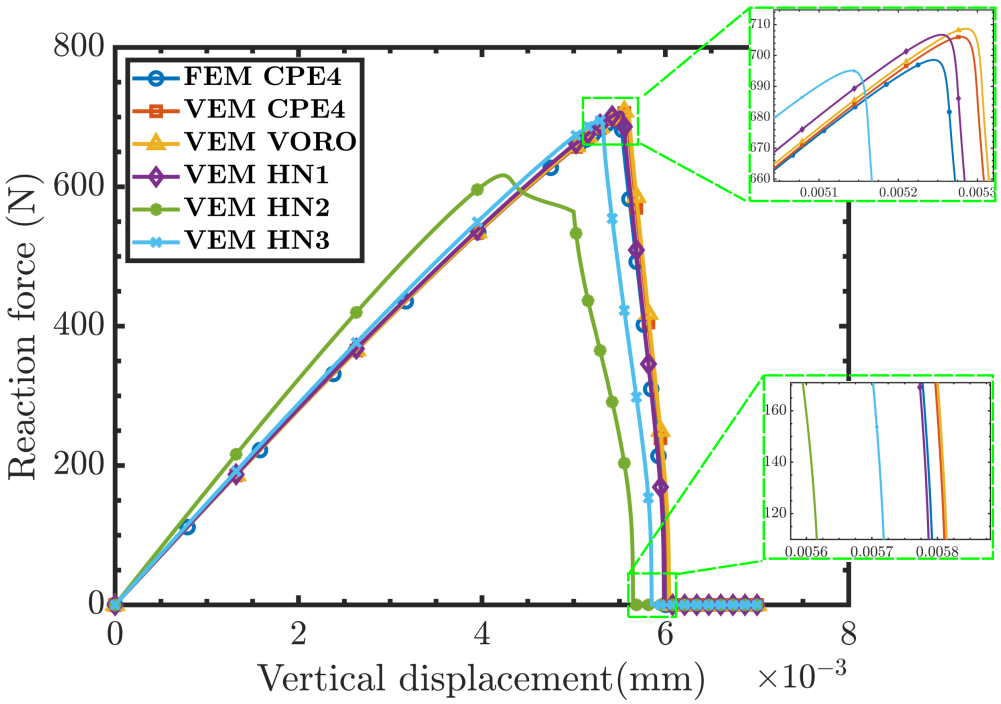

Figure 7: Reaction vs. displacement plot for different types of discretization

The crack initiation and subsequent crack propagation for the discretization VEM HN1 is compared with the discretization FEM CPE4 in Fig. 8. It can be observed that the presence of 13-noded and 6-noded transition elements in VEM HN does not affect the crack initiation load and crack propagation direction. In both the cases, the crack initiates at a displacement of $\bar{u} = 0.0056$ mm and propagates in a brittle manner until an applied displacement of $\bar{u} = 0.006$ mm leading to final failure.

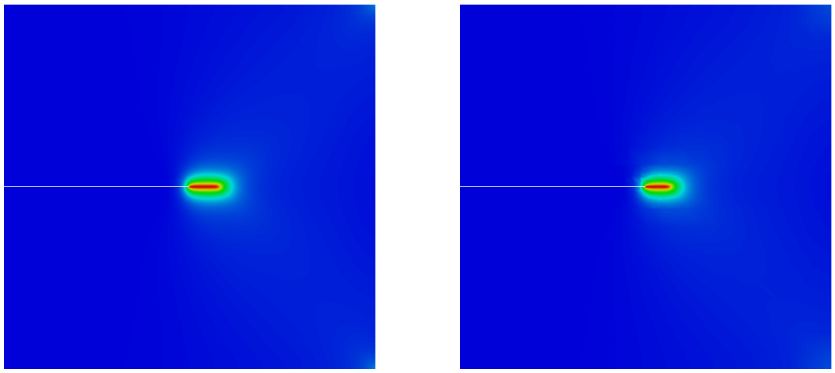

(a) FEM $\bar{u} = 0.0056$ mm

(b) VEM $\bar{u} = 0.0056$ mm

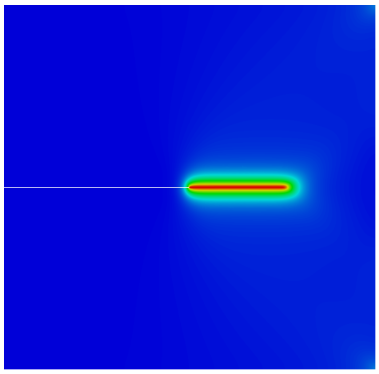

(c) FEM $\bar{u} = 0.0058$ mm

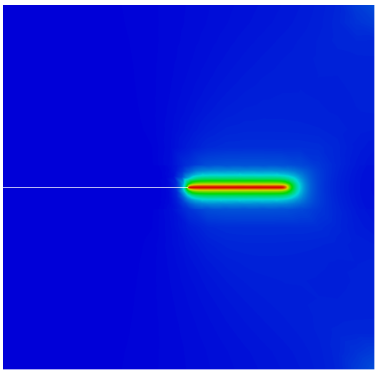

(d) VEM $\bar{u} = 0.0058$ mm

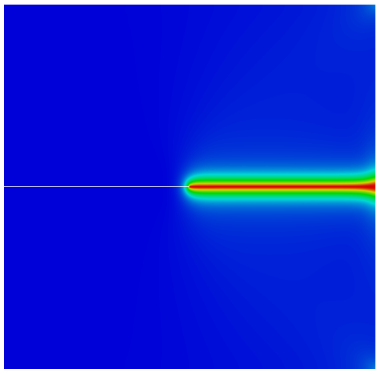

(e) FEM $\bar{u} = 0.006$ mm

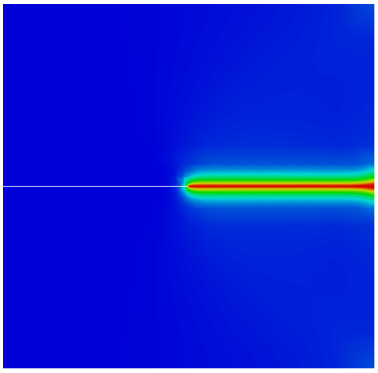

(f) VEM $\bar{u} = 0.006$ mm

Figure 8: Stages of crack propagation in SENT specimen at various applied displacement levels for the discretization FEM CPE4 (left) and VEM HN1 (right)

Finally, a comparison of the number of degrees of freedom and the CPU time is shown in Table 1. The results highlight the significant reduction of these measures by about 60 % achieved with the VEM HN1 discretization as compared to FEM CPE4. This is made possible by the strategic placement of the 13-noded and 6-noded transition elements, which enables rapid transition from fine mesh to coarse mesh, which would have been difficult to achieve with conventional FEM elements.

Table 1: Comparison of degrees of freedom and CPU time between FEM and VEM discretization

Discretization	**Number of nodes**	**CPU time (seconds)**
FEM CPE4	36708	2580
VEM HN1	12659 (**65%** ↓)	1140 (**56%** ↓)

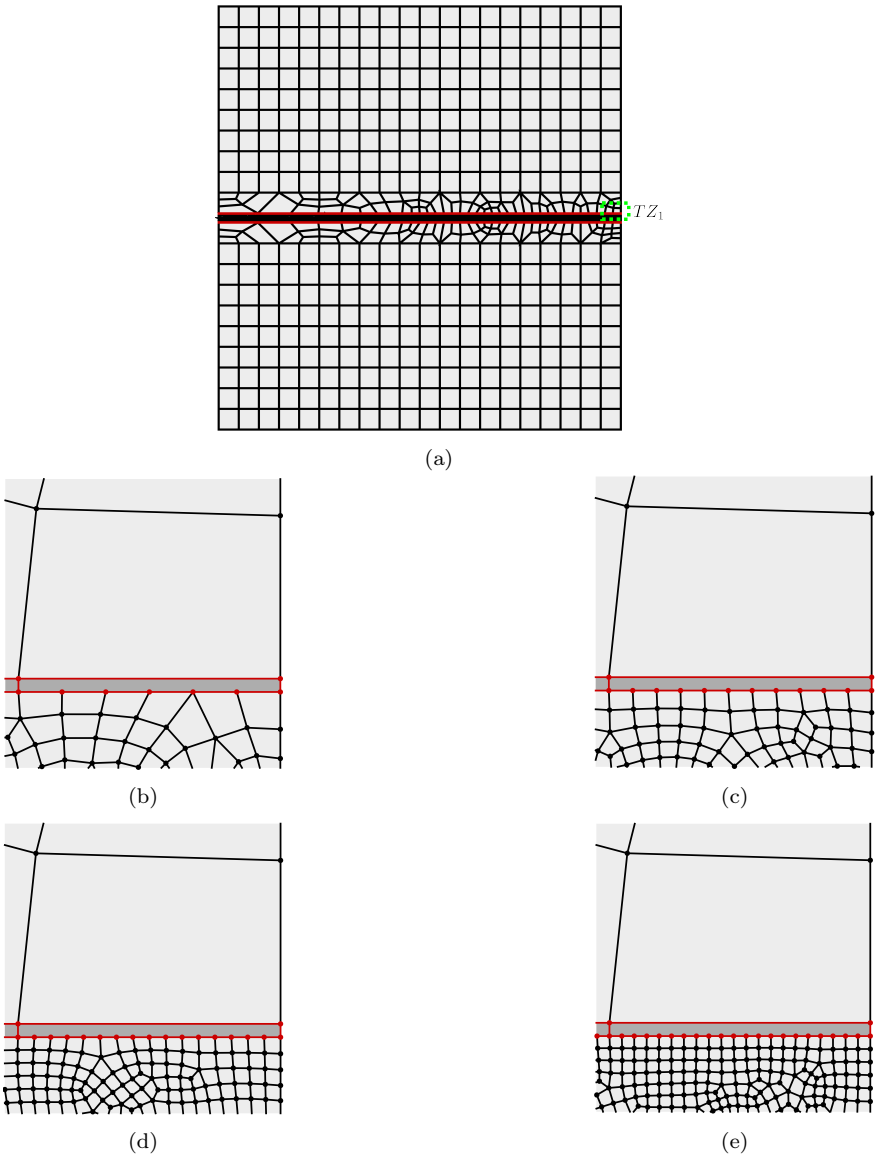

Figure 9: Discretization used to study the influence of hanging nodes (a) VEM mesh with the region TZ_1 highlighting the transition zone located at a distance of $0.67l_0$ from the centre. (b) TZ_1 region with 5 hanging nodes (b) TZ_1 region with 10 hanging nodes (b) TZ_1 region with 15 hanging nodes (b) TZ_1 region with 20 hanging nodes

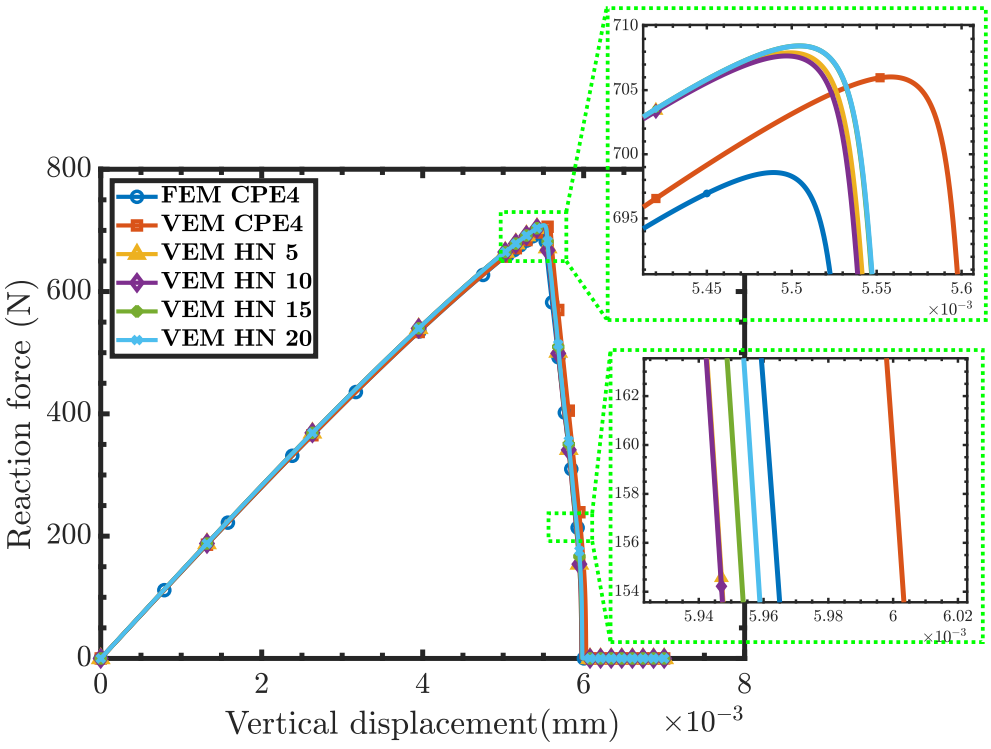

Figure 10: Reaction vs. displacement plot for different number of hanging nodes

4.1.1. Influence of the number of hanging nodes

We previously showed that for the VEM HN2 and VEM HN3 meshes, using single virtual elements with a large number of hanging nodes resulted in inaccuracies in both the peak load and the post-peak response. However, these inaccuracies might also be related to differences in element size between the two meshes. Therefore, we now isolate the influence of the number of hanging nodes by keeping the element size fixed and varying only the number of hanging nodes within the transition elements. Fig. 9 illustrates the discretization employed, with the region highlighted in red indicating the transition zone where hanging nodes are introduced. Figs. 9b – 9e present zoomed-in views of the region marked as TZ_1 in Fig. 9a. Specifically, these figures demonstrate how, with a constant element size, the number of hanging nodes along the bottom edge of the transition zone increases from 5 (Fig. 9b) to 20 (Fig. 9e). We denote each of these meshes as VEM HN 'x' mesh, where x denotes the number of hanging nodes. For example, VEM HN 5 mesh would refer to the mesh shown in Fig. 9b, which has 5 hanging nodes.

Fig. 10 presents the reaction versus displacement curves for VEM discretizations with meshes having hanging nodes ranging from 5 to 20. It can be observed that near the peak load, all meshes with hanging nodes yield slightly higher reaction forces compared to the FEM and VEM meshes without hanging nodes. Conversely, in the post-peak region,

Table 2: Comparison between number of nodes, reaction force and failure displacement for meshes with different number of hanging nodes. Values in brackets indicate the relative error with respect to the FEM mesh in case of peak reaction force and displacement at failure and % reduction in degrees of freedom for the case of number of nodes.

Discretization	**Number of nodes**	**Peak reaction Force (N)**	**Displacement at failure (mm)**
FEM CPE4	36708	698.574	6.002×10^{-3}
VEM CPE4	36708	706.032 (1.07%)	6.038×10^{-3} (0.60%)
VEM HN 20	14432 (60.68%)	707.913 (1.34%)	5.976×10^{-3} (-0.44%)
VEM HN 15	11917 (67.54%)	707.667 (1.30%)	5.976×10^{-3} (-0.44%)
VEM HN 10	8991 (75.51%)	708.452 (1.41%)	5.984×10^{-3} (-0.30%)
VEM HN 5	6134 (83.29%)	708.450 (1.41%)	5.984×10^{-3} (-0.21%)

meshes with hanging nodes exhibit an earlier failure than meshes without any hanging nodes. These observations are quantitatively summarized in Table 2, which provides a detailed comparison between the number of nodes, peak reaction force, and displacement at failure for meshes with varying numbers of hanging nodes. The reduction in degrees of freedom achieved ranges from 60.68% for the VEM HN 20 mesh to 83.29% for the VEM HN 5 mesh. Importantly, the errors in peak reaction force and displacement at failure remain below 2%. These results demonstrate that acceptable accuracy can be maintained even with an increased number of hanging nodes, provided the element size remains constant, at least in the Mode-I dominated fracture scenario considered here (SENT specimen). However, it should be noted that the post-peak response may differ somewhat from that obtained with conventional finite elements. Further discussions on more complex loading conditions, including mixed-mode fracture cases, are presented in Section 4.2.

4.2. Refinement strategy

Section 4.1 thus shows that, though VEM provides immense flexibility in the choice of element shape, it can lead to inaccurate results when an element with too many hanging nodes is used in phase-field fracture simulations. In this section, we provide some guidelines on choosing the mesh transition rates, number of hanging nodes and their placement with respect to the crack front so that the results can be achieved with acceptable accuracy.

4.2.1. Effect of mesh transition rate

We now conduct extensive numerical studies to evaluate the accuracy of the virtual element method for the following three different mesh transition rates:

- 3:1 transition ($\mathcal{T}_1$), where the mesh is graded from 3 fine elements to 1 coarse element with 2 hanging nodes.
- 7:1 transition ($\mathcal{T}_2$), where the mesh is graded from 7 fine elements to 1 coarse element with 6 hanging nodes
- 11:1 transition ($\mathcal{T}_3$), where the mesh is graded from 11 fine elements to 1 coarse element with 10 hanging nodes

We use the K-field displacement loading to study the effect of these transition rates under Mode-I as well as mixed mode loading conditions. In LEFM, the K-field loading refers to the application of load as a function of stress intensity factors that characterize the singular stress fields near the crack tip under mixed-mode loading conditions. The far-field displacement loading for an infinite domain with a pre-existing crack that leads to a singular state of stress at the crack tip can be expressed as [30]

$$\begin{aligned} u_x = \frac{K_I}{\mu}\sqrt{\frac{R}{2\pi}}\cos\frac{\theta}{2}\left(2(1-\nu)-\cos^2\frac{\theta}{2}\right) \\ + \frac{K_{II}}{\mu}\sqrt{\frac{R}{2\pi}}\sin\frac{\theta}{2}\left(2(1-\nu)+\sin^2\frac{\theta}{2}\right) \end{aligned} \tag{38a}$$

$$\begin{aligned} u_y = \frac{K_I}{\mu}\sqrt{\frac{R}{2\pi}}\sin\frac{\theta}{2}\left(2(1-\nu)-\cos^2\frac{\theta}{2}\right) \\ - \frac{K_{II}}{\mu}\sqrt{\frac{R}{2\pi}}\cos\frac{\theta}{2}\left(-2\nu+\cos^2\frac{\theta}{2}\right) \end{aligned} \tag{38b}$$

where, u_x, u_y are the x and y displacements, K_I, and K_{II} are the mode-I and mode-II stress-intensity factors. R and θ are the polar coordinates measured with respect to the origin located at the notch tip. μ and ν are the shear modulus and the poisson's ratio of the material respectively. The singular stress distribution resulting from the displacement field (Eq. 38) takes the form

$$\begin{aligned} \sigma_{xx} = \frac{K_I}{\sqrt{2\pi R}}\cos\frac{\theta}{2}\left(1-\sin\frac{\theta}{2}\sin\frac{3\theta}{2}\right) \\ - \frac{K_{II}}{\sqrt{2\pi R}}\sin\frac{\theta}{2}\left(2+\cos\frac{\theta}{2}\cos\frac{3\theta}{2}\right) \end{aligned} \tag{39a}$$

$$\begin{aligned} \sigma_{yy} = \frac{K_I}{\sqrt{2\pi R}}\cos\frac{\theta}{2}\left(1+\sin\frac{\theta}{2}\sin\frac{3\theta}{2}\right) \\ + \frac{K_{II}}{\sqrt{2\pi R}}\sin\frac{\theta}{2}\cos\frac{\theta}{2}\cos\frac{3\theta}{2} \end{aligned} \tag{39b}$$

A schematic of the boundary value problem is shown in Fig. 11. The problem consists of a 2D square domain of dimensions $800l_0 \times 800l_0$. A pre-existing crack of length $200l_0$, starting from the left boundary and placed mid-height exists in the centre of the domain. A portion of the crack of length $3l_0$ starting from the geometrical notch tip is given a diffused representation [28]. This makes the crack nucleate around $G = 1.2G_c$. The origin is located at the crack tip. The elastic and fracture material properties are taken to be $\mu = 76923\ \mathrm{N}/mm^2$, $\nu = 0.3$, $G_c = 3.033\ \mathrm{N/mm}$ and $l_0 = 0.5$ mm. The mesh size near the notch (h_0) is taken to be 0.05 mm, resulting in a l_0/h_0 ratio of 10. is The K field displacement described by Eq. 38 is applied to the boundary of the domain. Two sets of simulations are performed

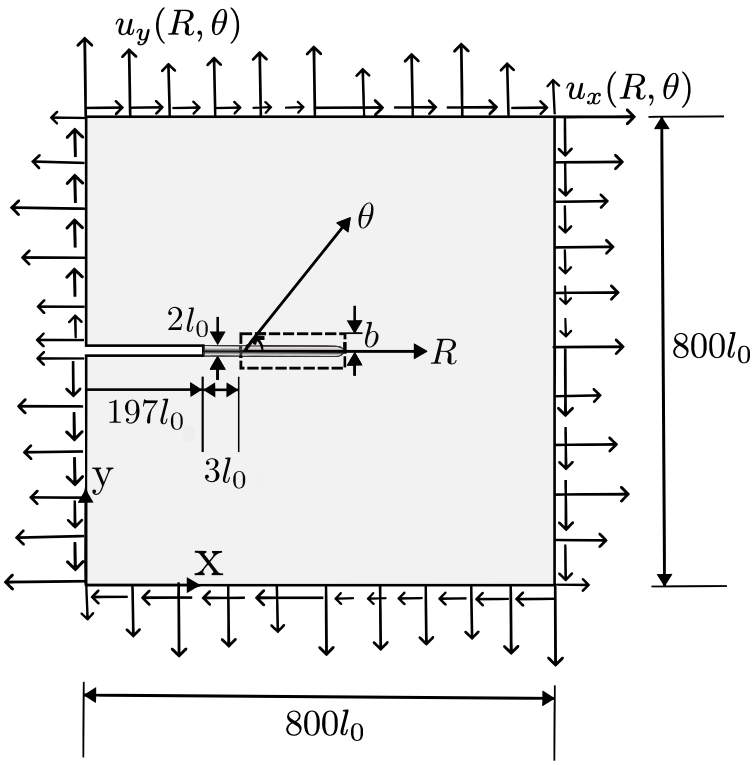

Figure 11: Domain with K-field applied boundary condition

- (S1) Mode I simulations ($K_{II} = 0$) using virtual elements with the mesh transition rates $\mathcal{T}_1, \mathcal{T}_2$ and $\mathcal{T}_3$. The ratio $\frac{b}{l_0}$ is used to paramterise the location of transition elements with repect to the crack front. Here, b represents the vertical distance from the crack front ($\theta = 0$ axis). Five different values of $\frac{b}{l_0}$ are chosen, which are 1, 0.8, 0.6, 0.4 and 0.2.

- (S2) With the number of hanging nodes and the ratio $\frac{b}{l_0}$ determined from S1, mixed-mode simulations are performed for the mode-mixity, $\gamma = 0$, 0.22, 0.53 and 1, where $\gamma = \frac{K_{II}}{K_I + K_{II}}$.

The meshes used for the simulations S1 corresponding to $b/l_0 = 1$, 0.6, 0.2 for the three different mesh transition rates $\mathcal{T}_1$, $\mathcal{T}_2$ and $\mathcal{T}_3$ are shown in Fig. 12. Fig. 12j shows the damage contour on a mesh with no transition elements. The final values of the developed phase-field is similar in all these meshes indicating no loss of accuracy in the computation of primary field variables.

Fig. 13 shows the displacement profile of the top crack face for the mesh transition rates, $\mathcal{T}_1$ (Fig. 13a), $\mathcal{T}_2$ (Fig. 13b) and $\mathcal{T}_3$ (Fig. 13c). For each mesh transition rate, comparisons are made between VEM mesh with transition elements placed at different values of $\frac{b}{l_0}$, VEM and FEM mesh with only quadrilateral elements and LEFM analytical solutions. From Fig. 13a, 13b and 13c, it can be observed that though there is a difference between the displacement profiles of the VEM mesh and LEFM analytical results at distances closer to

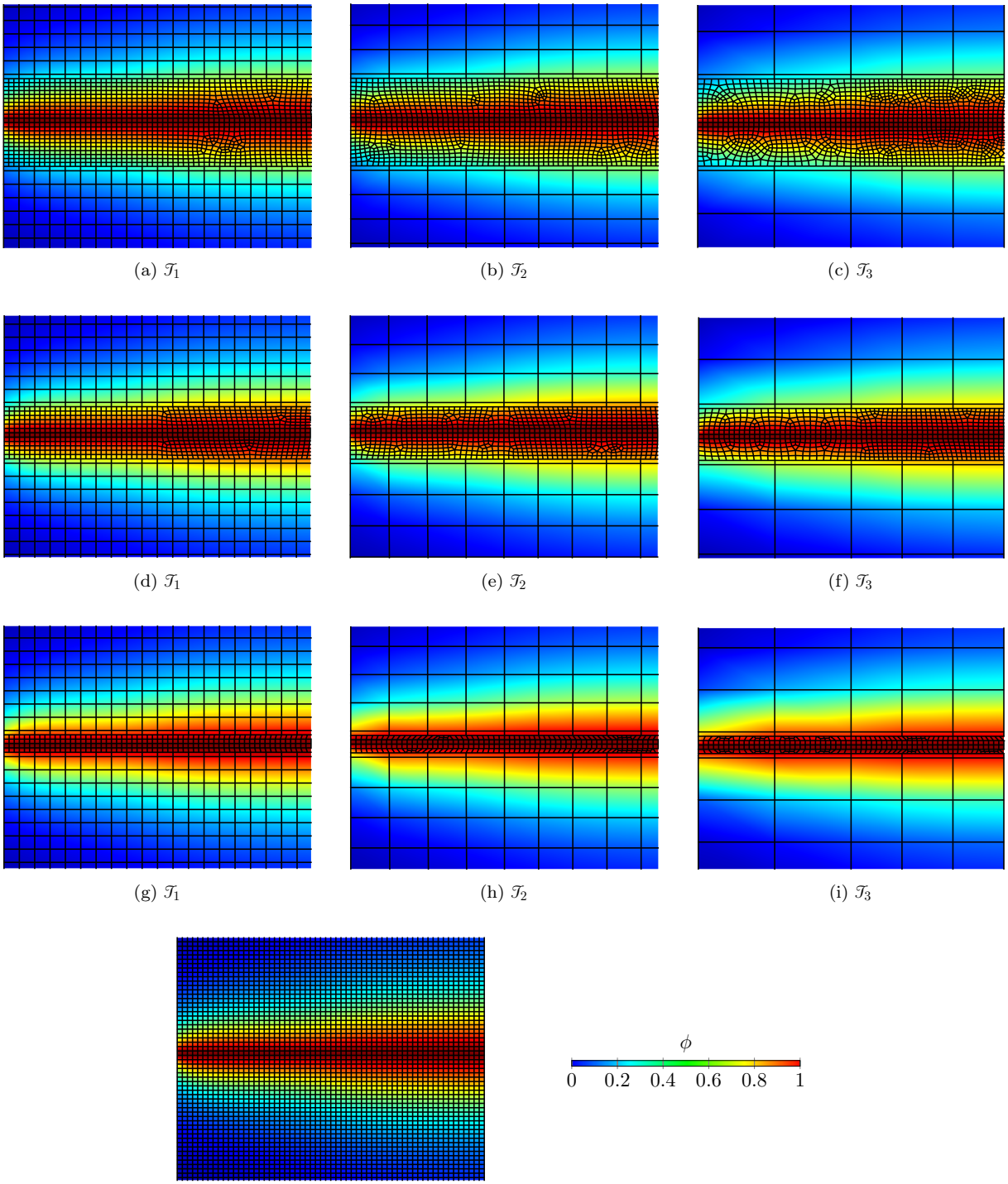

(a) $\mathcal{T}_1$ (b) $\mathcal{T}_2$ (c) $\mathcal{T}_3$

(d) $\mathcal{T}_1$ (e) $\mathcal{T}_2$ (f) $\mathcal{T}_3$

(g) $\mathcal{T}_1$ (h) $\mathcal{T}_2$ (i) $\mathcal{T}_3$

(j) 4-noded quadrilateral VEM mesh

Figure 12: Zoomed in view of the mesh used in S1 simulations near the crack front along with the final phase-field values for mesh transitions rates $\mathcal{T}_1$, $\mathcal{T}_2$ and $\mathcal{T}_3$ corresponding to three different values of $\frac{b}{l_0}$ (a-c) $b/l_0 = 1$, (d-f) $b/l_0 = 0.6$ and (g-i) $b/l_0 = 0.2$ (j) reference VEM mesh with 4-noded quadrilateral elements

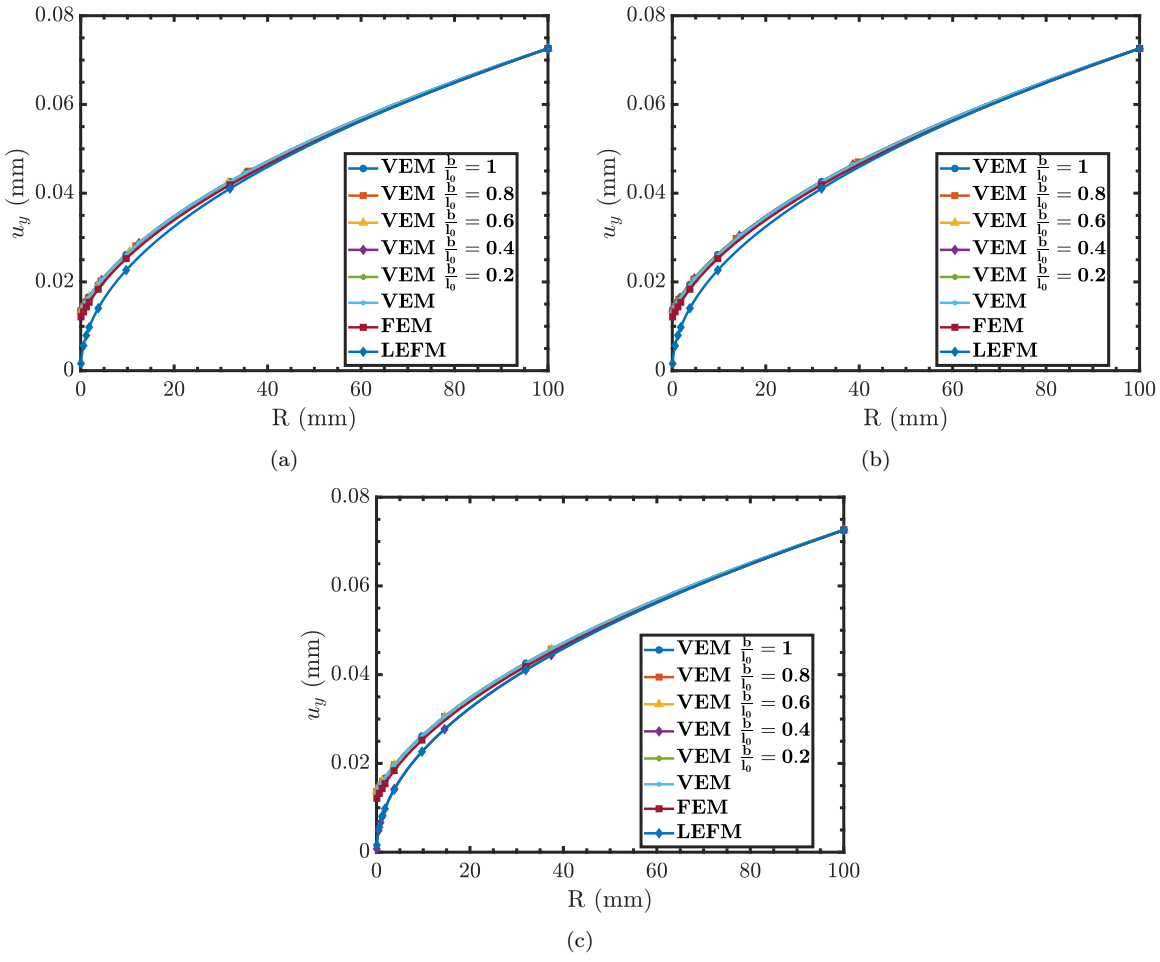

Figure 13: Comparison of u_y at the top crack face with FEM and LEFM for several values of $\frac{b}{l_0}$ for the three different mesh transition rates (a) $\mathcal{T}_1$ (b) $\mathcal{T}_2$ (c) $\mathcal{T}_3$

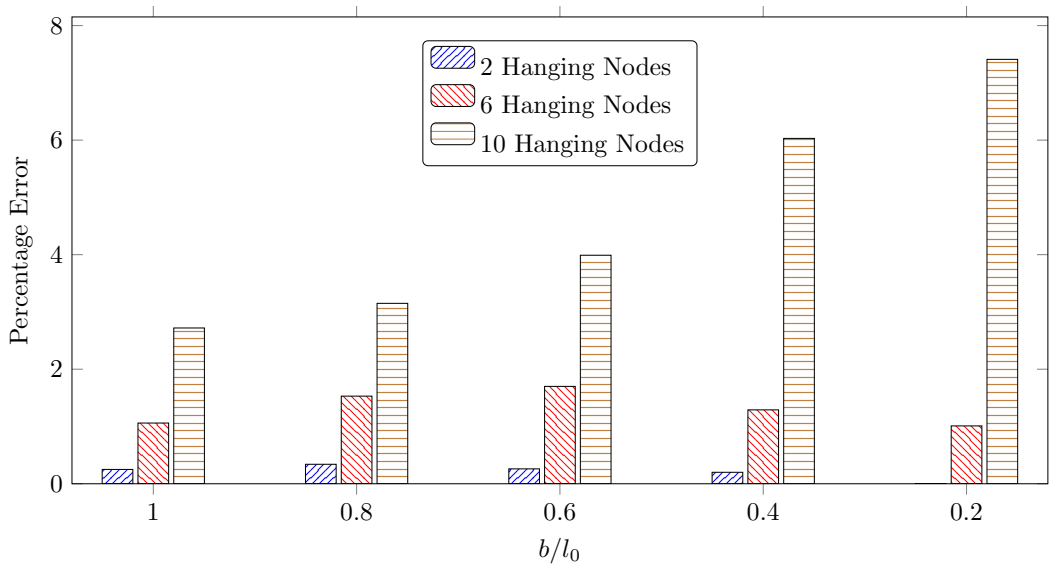

Figure 14: Percentage error in the peak vertical stress at the crack front in Mode I fracture for different number of hanging nodes and $\frac{b}{l_0}$ value.

the wake of the crack, the differences become negligibly small at distances farther away from the notch. This is due to the presence of the finite size of process zone near the crack tip in a phase-field description of brittle fracture. Interestingly, the position of transition elements with respect to the crack front ($\frac{b}{l_0}$) doesn't affect the displacement profiles for any mesh transition rate.

Fig. 14 shows the percentage error in the peak vertical stress σ_{yy} at the crack front relative to the VEM mesh with only quadrilateral elements. It can be observed that the error increases as the mesh transition becomes more rapid and when the transition elements are placed closer to the crack front (i.e., lower $\frac{b}{l_0}$ value). Thus, to obtain a reasonable prediction of the peak load, it is essential to restrict the mesh transition rate and the placement of transition elements with respect to the crack front. Thus, while making mesh transition we recommend placing the transition elements atleast at a distance of $0.6l_0$ from the crack front. Furthermore, we recommend choosing transition rates $\mathcal{T}_2$ or $\mathcal{T}_1$ to keep the peak stress error under 2 percent while doing Mode-I phase-field fracture simulations.

We now choose the mesh transition rate $\mathcal{T}_2$ and keep the transition elements at $0.6l_0$ from the crack front to study the effects of mixed-mode loading conditions for simulations S2. The crack kinking angle obtained with the mesh transition rate $\mathcal{T}_2$ is compared to the crack kinking angle obtained using the maximum energy release rate (ERR) criterion. Fig. 15 shows the phase-field damage contours for different values of mode-mixity as characterized by γ. Fig. 16 highlights that even in the presence of transition elements, the crack kinking angle is in good agreement with the maximum ERR criteria. This suggests that the local stress state at crack initiation, which governs the crack kinking angle, remains unaffected

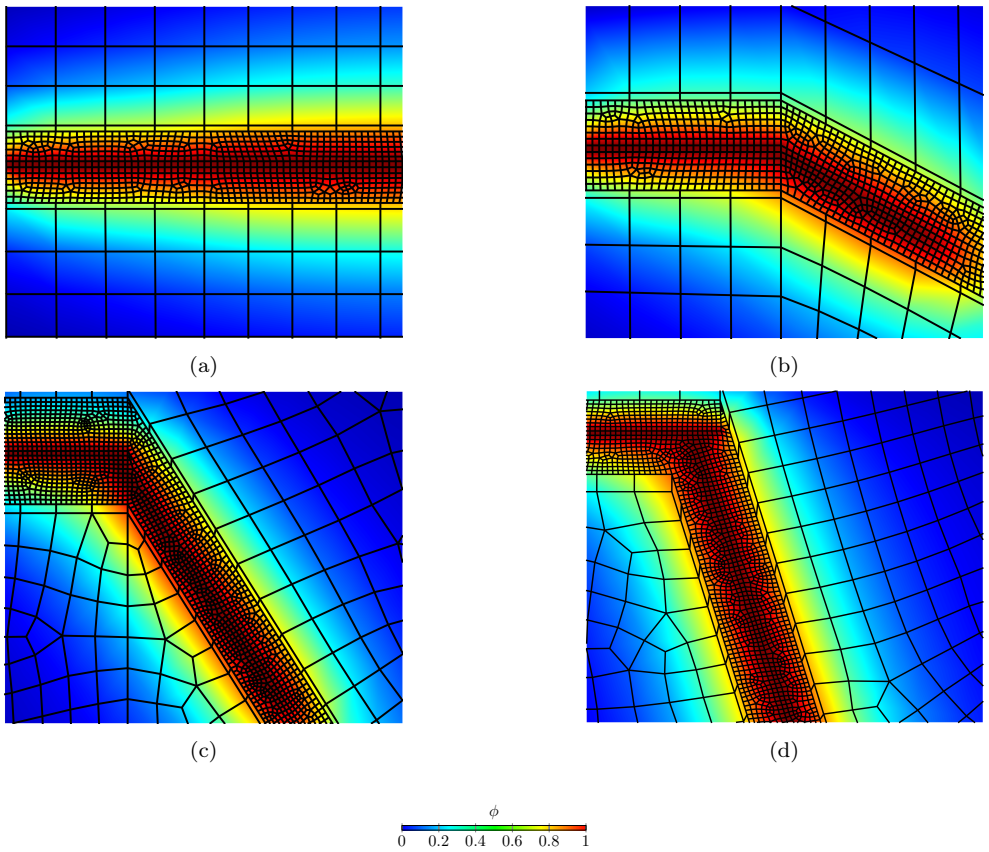

Figure 15: Damage contours showing crack kinking for various values of $\gamma = \frac{K_{II}}{K_I+K_{II}}$ for number of hanging nodes = 6 and $\frac{b}{l_0} = 0.6$ (a) $\gamma = 0$ (b) $\gamma = 0.22$ (c) $\gamma = 0.53$ (d) $\gamma = 1$

by the mesh transition rate $\mathcal{T}_2$.

Though the crack kinking angle indicates the local stress states are captured properly with the mesh transition rate $\mathcal{T}_2$, it doesn't give much information about the accuracy with which global stress or strain states are evaluated. To understand the global response under mixed mode loading conditions, we compute the projected surface energy of the discretised assembly for the mesh transition rates $\mathcal{T}_1$, $\mathcal{T}_2$ and $\mathcal{T}_3$ corresponding to $b/l_0 = 0.6$. The projected surface energy, which is a measure of the energy dissipated due to damage, is given as:

$$\mathbf{\Pi}_\phi^\nabla \hat{\psi}^{frac} = \sum_N \int_E \frac{G_c}{2l_0} \left(\left(\Pi_\phi^\nabla(\phi)\right)^2 + l_0^2 \nabla \Pi_\phi^\nabla(\phi) \cdot \nabla \Pi_\phi^\nabla(\phi) \right) dE. \tag{40}$$

Fig. 17 shows the projected surface energy, $\mathbf{\Pi}_\phi^\nabla \hat{\psi}^{frac}$ over the time history of loading for $b/l_0 = 1$ for different mesh transition rates. It should be noted that until a pseudo time value of $1s$, only the phase-field develops in the pre-defined notch region (i.e. no K-field loading conditions is applied). For all the mesh transition rates $\mathcal{T}_1$, $\mathcal{T}_2$ and $\mathcal{T}_3$, $\mathbf{\Pi}_\phi^\nabla \hat{\psi}^{frac}$ is almost the same as the corresponding VEM or FEM mesh with no transition elements until

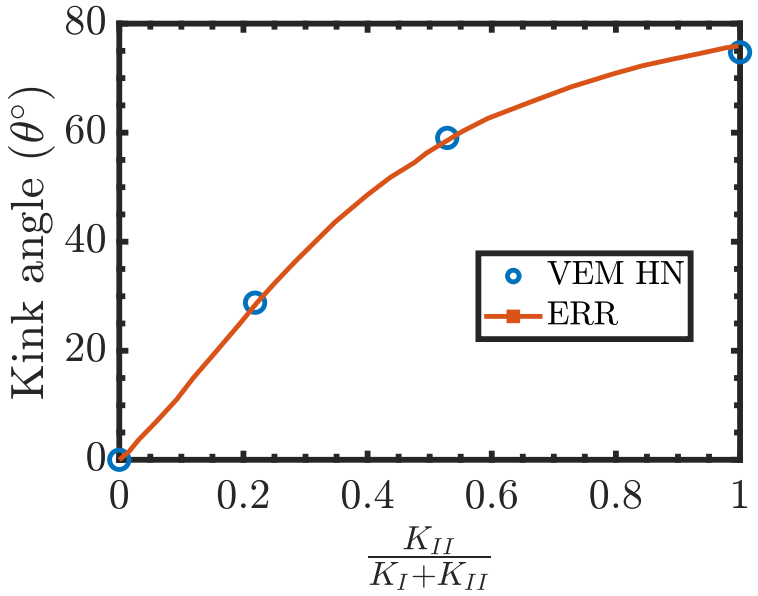

Figure 16: Comparison of crack kinking angle with maximum energy release rate (ERR) criterion

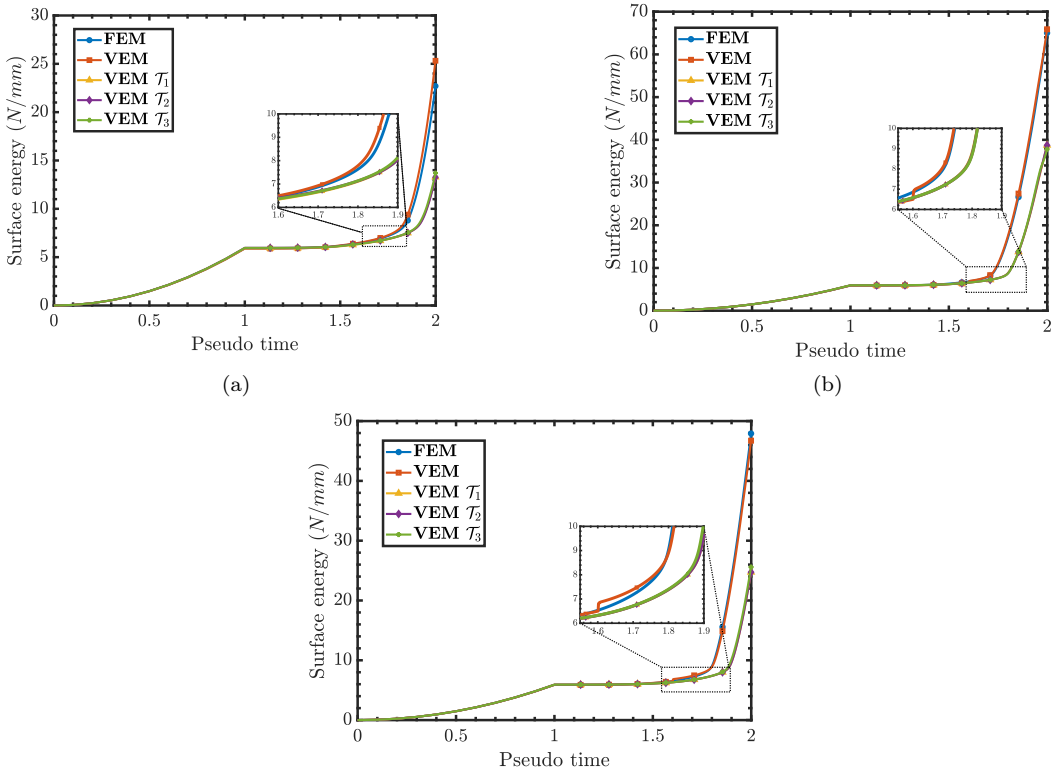

Figure 17: Surface energy for various values of $\gamma = \frac{K_{II}}{K_I+K_{II}}$ for different mesh transition rates and $\frac{b}{l_0} = 0.6$ (a) $\gamma = 0.22$ (b) $\gamma = 0.53$ (c) $\gamma = 1$

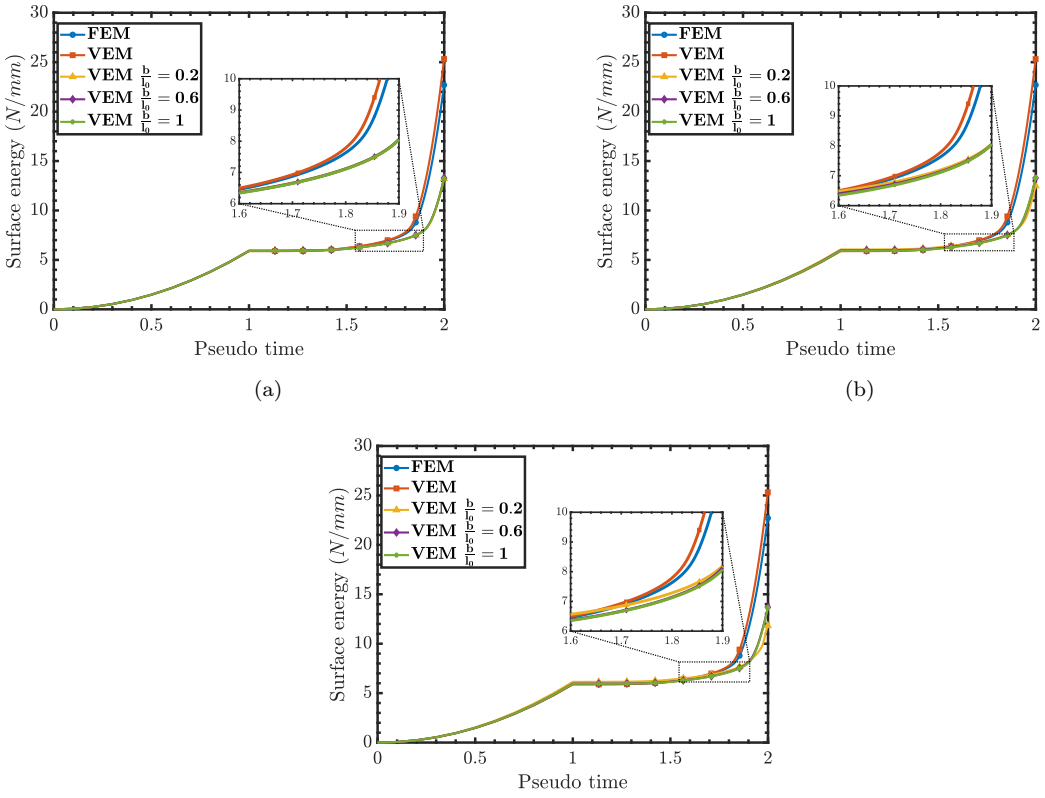

Figure 18: Surface energies for different mesh transition rates for several values of b/l_0 ratios corresponding to $\gamma = 0.22$ (a) $\mathcal{T}_1$ (b) $\mathcal{T}_2$ (c) $\mathcal{T}_3$

the process of crack initiation. This probably explains why the crack kinking angle was captured correctly for all the mesh transition rates. Once the crack initiates, $\mathbf{\Pi}_{\phi}^{\nabla}\hat{\psi}^{frac}$ is under-predicted, albeit by the same amount in all three mesh transition rates. Thus, while using transition elements, the post-peak response can show a slightly different behavior as compared to meshes without transition elements.

Figs. 18, 19, and 20 illustrate the evolution of surface energies for various b/l_0 ratios at mode-mixity (γ) values of 0.22, 0.53, and 1, respectively. Each figure compares results obtained using three mesh transition rates: $\mathcal{T}_1$, $\mathcal{T}_2$, and $\mathcal{T}_3$. It is evident that all considered mesh transition rates ($\mathcal{T}_1$, $\mathcal{T}_2$, and $\mathcal{T}_3$) consistently under-predict surface energies relative to the conventional 4-noded finite element solutions across all mode-mixities. The influence of the b/l_0 ratio is particularly pronounced for the most abrupt transition rate $\mathcal{T}_3$ (Figs. 18c, 19c, 20c). Specifically, an abrupt mesh transition rate ($\mathcal{T}_3$) located closer to the crack front (e.g., $b/l_0 = 0.2$) significantly increases the under-prediction of surface energy post-crack initiation. Conversely, for less abrupt transition rates ($\mathcal{T}_1$ and $\mathcal{T}_2$), the placement of the transition region does not noticeably impact surface energy evolution. Thus, it is advisable to avoid mesh transition rates more abrupt than $\mathcal{T}_2$ to ensure accurate prediction of surface energy evolution.

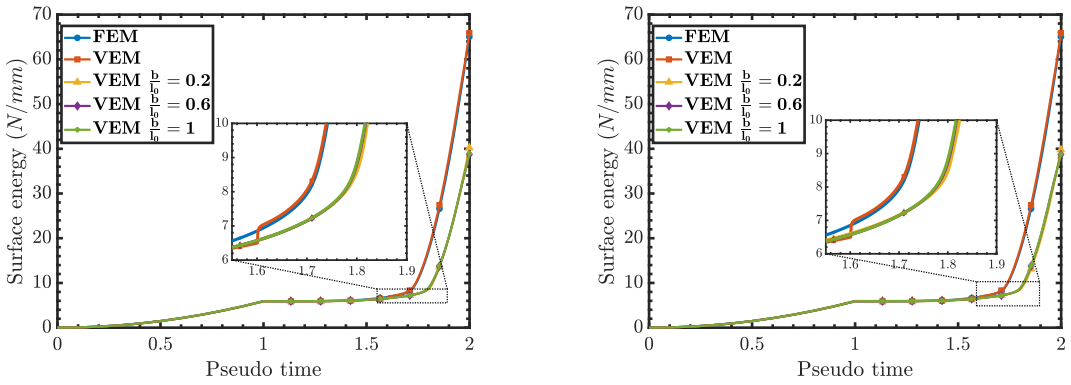

(a) (b)

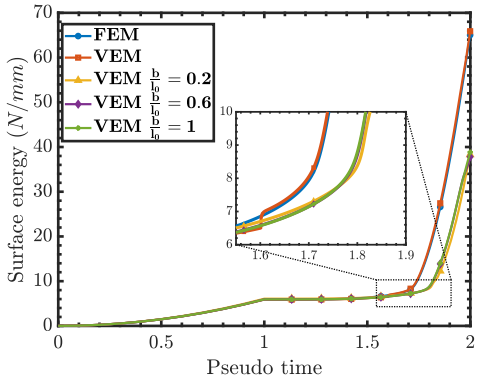

(c)

Figure 19: Surface energies for different mesh transition rates for several values of b/l_0 ratios corresponding to $\gamma = 0.53$ (a) $\mathcal{T}_1$ (b) $\mathcal{T}_2$ (c) $\mathcal{T}_3$

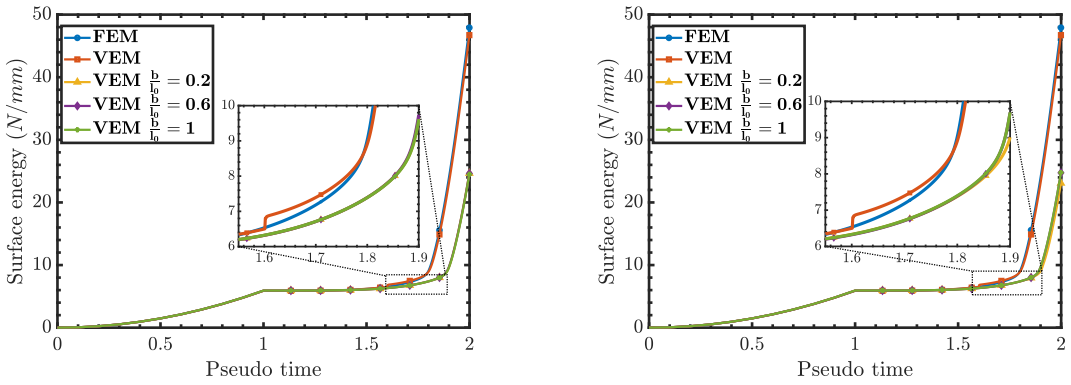

(a) (b)

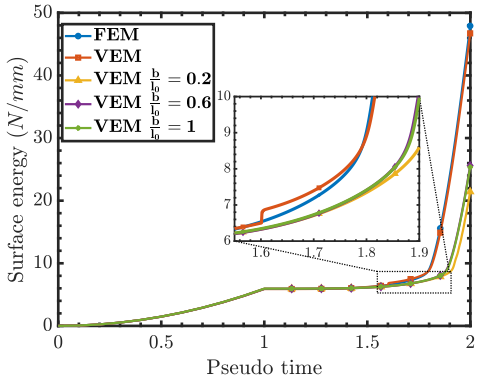

(c)

Figure 20: Surface energies for different mesh transition rates for several values of b/l_0 ratios corresponding to $\gamma = 1$ (a) $\mathcal{T}_1$ (b) $\mathcal{T}_2$ (c) $\mathcal{T}_3$

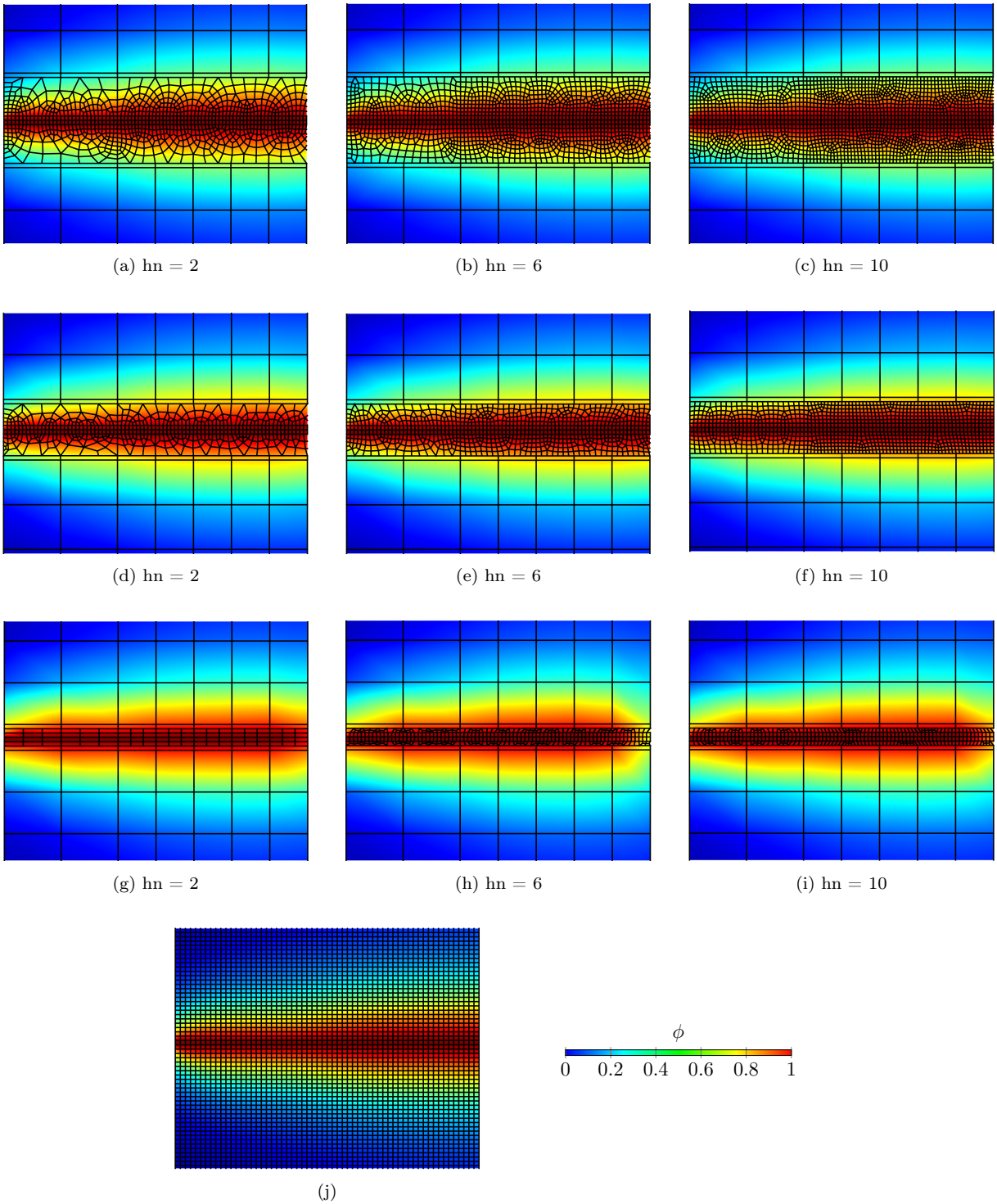

Figure 21: Zoomed in view of the mesh used in mode I simulations near the crack front along with the final phase-field values for number of hanging nodes (hn) = 2, 6 and 10 corresponding to three different values of $\frac{b}{l_0}$ (a-c) $b/l_0 = 1$, (d-f) $b/l_0 = 0.6$ and (g-i) $b/l_0 = 0.2$ (j) reference VEM mesh with 4-noded quadrilateral elements

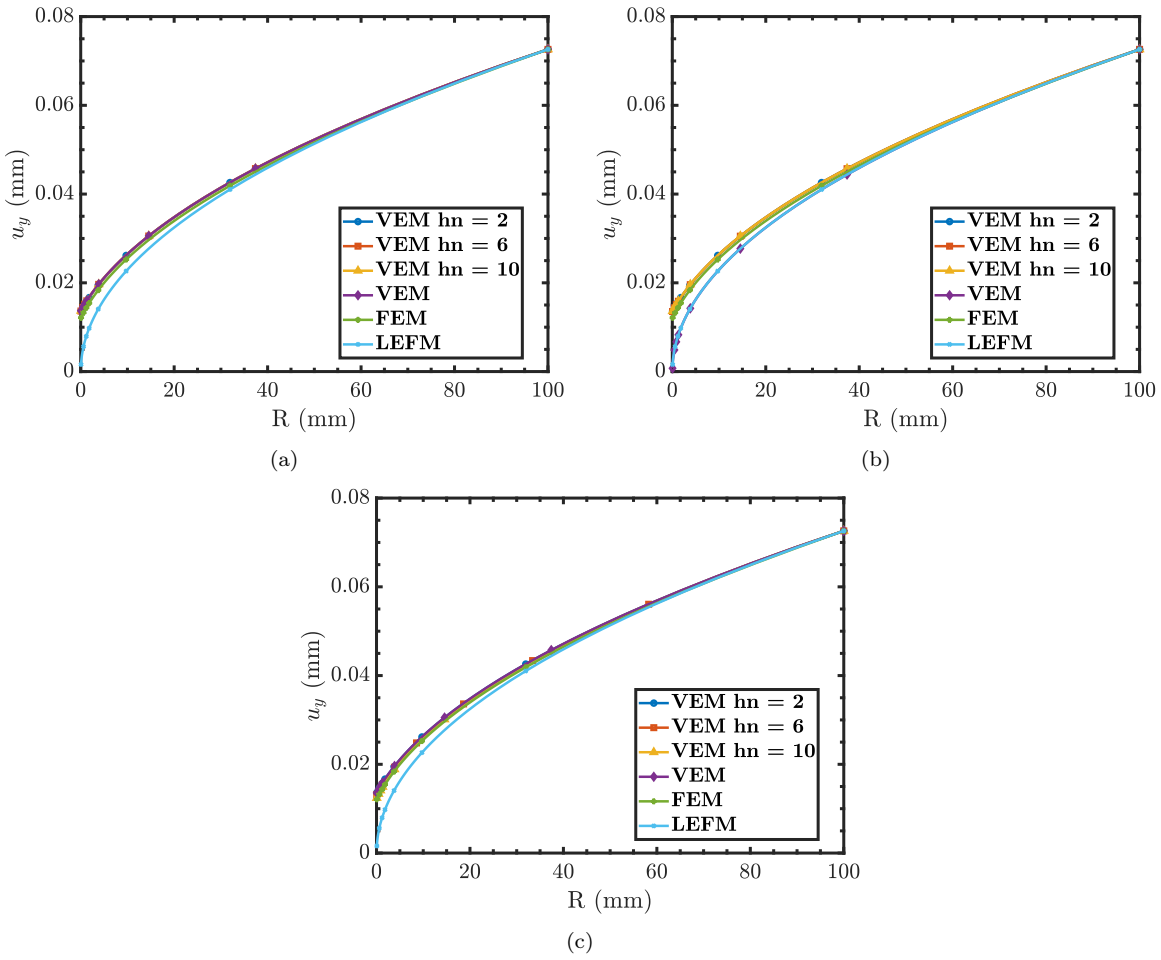

Figure 22: Comparison of u_y at the top crack face with FEM and LEFM for several values of $\frac{b}{l_0}$ with different number of hanging nodes (a) $\frac{b}{l_0} = 0.2$ (b) $\frac{b}{l_0} = 0.6$ (c) $\frac{b}{l_0} = 1.0$

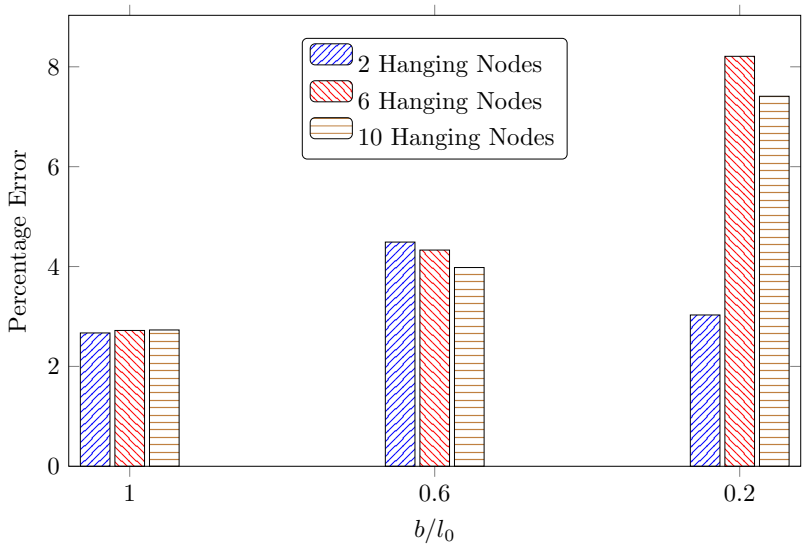

Figure 23: Percentage error in the peak vertical stress at the crack front in Mode I fracture for different number of hanging nodes and $\frac{b}{l_0}$ value.

4.2.2. Effect of number of hanging nodes

We now keep the size of the coarse element constant and subsequently introduce hanging nodes to isolate the effect of hanging nodes on the solution accuracy under mode I and mixed-mode loading conditions. The domain size is kept the same as in Section 4.2.1. We consider the effect of adding 2, 6 and 10 hanging nodes at distances, $b = 0.2l_0$, $0.6l_0$ and $1l_0$ from the crack front.

The meshes used in the simulation are shown in Fig. 21. Similar to Section 4.2.1, it can be observed that the primary variables in the meshes with hanging nodes, which are the phase-field and displacement, remain the same as the VEM or FEM mesh with no hanging nodes. This is evident from the damage contours plotted over the meshes in Fig. 21 and displacement field of the top crack face in Fig. 22. However, the quantities that involve gradients, such as the stress, show error. This is evident from Fig. 23, which shows the percentage error in the peak stress ahead of a crack with respect to a mesh with no hanging nodes. It must be noted that unlike Section 4.2.1, where the mesh size was kept the same within a distance $\pm b$ from the crack front, the mesh size in these simulations is not the same in this zone. From Fig. 23 it can be seen that the incorporation of any number of hanging nodes leads to error of atleast 4 percent in the peak stress for $\frac{b}{l_0} = 0.6, 0.2$. However, for $\frac{b}{l_0} = 1$, the error of around 2.5 percent is nearly insensitive to the number of hanging nodes.

We fix the value of $\frac{b}{l_0} = 1$ and perform mixed mode simulations for 2, 6 and 10 hanging nodes for the mode-mixity ratios $\gamma = 0.22, 0.53, 1$. The meshes used in the simulation along with the phase-field contours is shown in Fig. 24. The last row of the Fig. 24 shows the phase-field contours plotted on a VEM mesh with no hanging nodes. It can be observed that

in all the cases of mesh with hanging nodes, the crack kinking angle is captured correctly. We have found in our simulation that the final crack lengths for the VEM mesh with hanging nodes were lesser as compared to the VEM mesh with no hanging nodes. The reason for this behavior is shown in Fig. 25, where it can be observed that the surface energy, $\mathbf{\Pi}_{\phi}^{\nabla}\hat{\psi}^{frac}$ for all the VEM meshes with hanging nodes deviates from the VEM mesh with no hanging nodes beyond the point of crack initiation for all mode-mixity ratios.

We now examine the effect of the $\frac{b}{l_0}$ ratio on the evolution of surface energy for various mode-mixity values and numbers of hanging nodes. Figs. 26, 27, and 28 illustrate the surface energy evolution corresponding to mode-mixity values (γ) of 0.22, 0.53, and 1.0, respectively. For each mode-mixity, we analyze the evolution of surface energy across different $\frac{b}{l_0}$ ratios for configurations with 2 (Figs. 26a, 27a, 28a), 6 (Figs. 26b, 27b, 28b), and 10 (Figs. 26c, 27c, 28c) hanging nodes. In all cases studied, the surface energies obtained with hanging nodes are consistently lower than those predicted by conventional four-noded FEM elements. Notably, placing hanging nodes closer to the crack front at a distance of $0.2l_0$ exacerbates the under-prediction. Conversely, positioning the hanging nodes at least $0.6l_0$ away from the crack front results in minimal changes to the evolution of surface energy, suggesting that increased distances from the crack front mitigate adverse effects on accuracy.

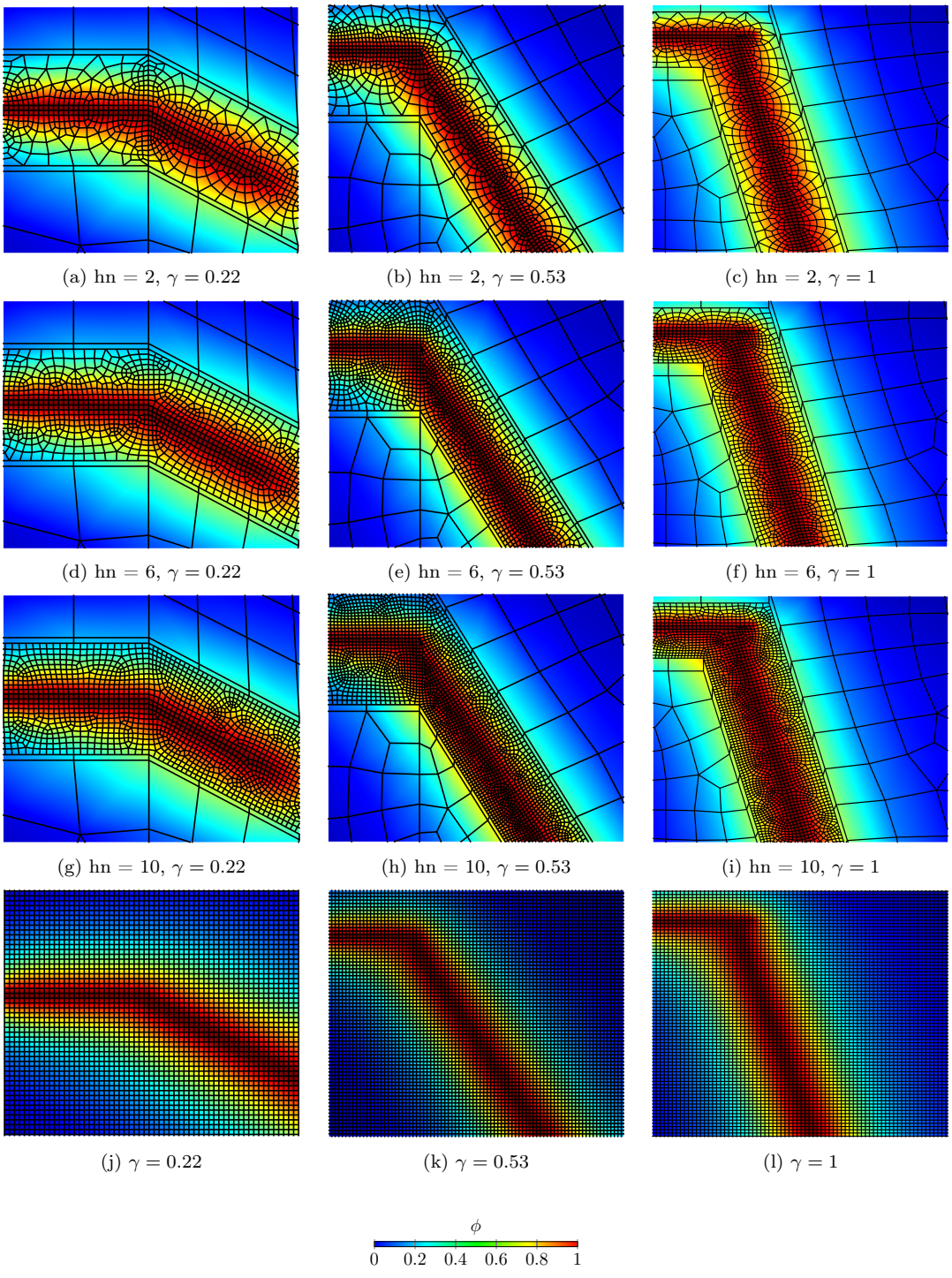

Figure 24: Zoomed in view of the mesh used in mixed mode simulations near the crack front along with the final phase-field values corresponding to $b/l_0 = 1$ and different number of hanging nodes (hn) (a-c) hn = 2, (d-f) hn = 6 and (g-i) hn = 10 (j-l) reference VEM mesh with no hanging nodes

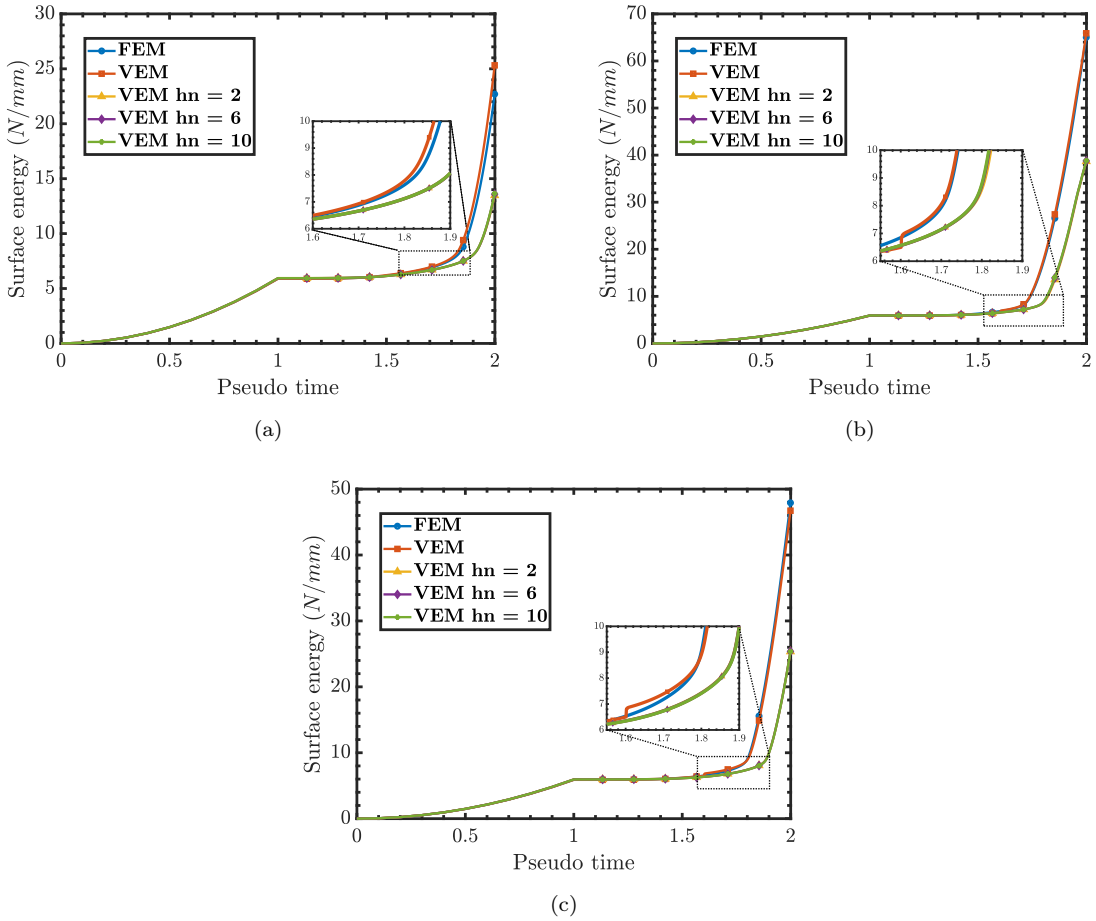

Figure 25: Surface energy corresponding to and $\frac{b}{l_0} = 1$ for various values of $\gamma = \frac{K_{II}}{K_I + K_{II}}$ for number of hanging nodes = 2, 6 and 10 (a) $\gamma = 0.22$ (b) $\gamma = 0.53$ (c) $\gamma = 1$

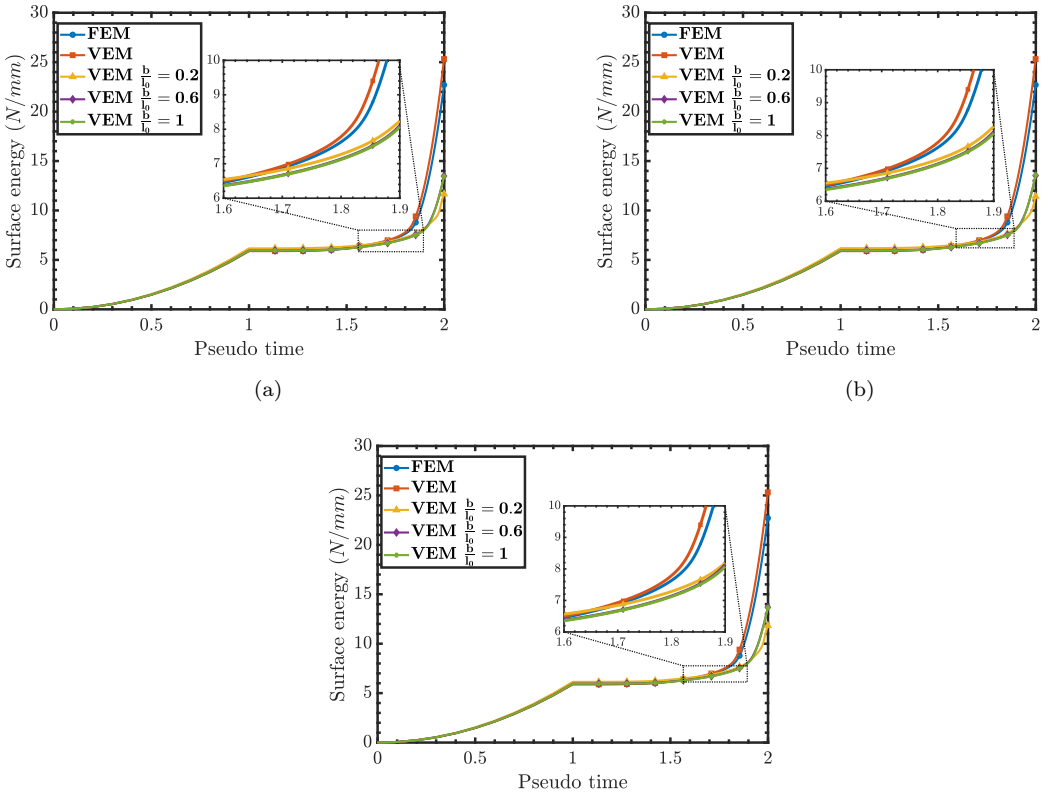

Figure 26: Surface energies for various values of b/l_0 ratios for different number of hanging nodes (hn) corresponding to $\gamma = 0.22$ (a) hn $= 2$ (b) hn $= 6$ (c) hn $= 10$

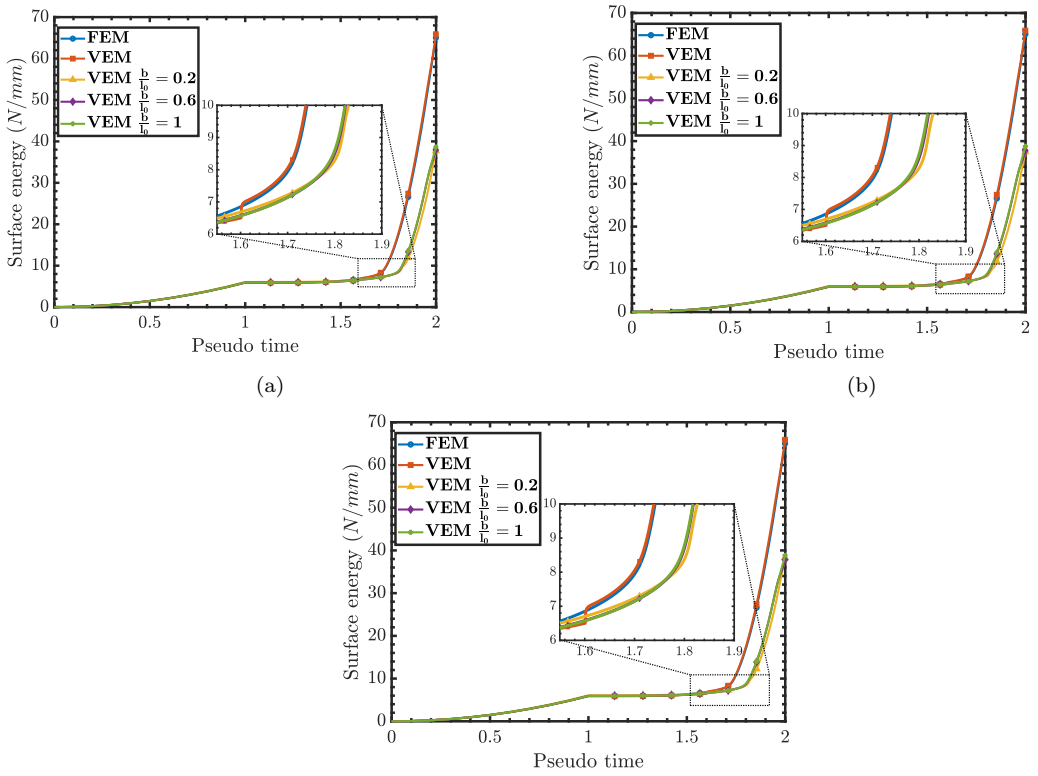

Figure 27: Surface energies for various values of b/l_0 ratios for different number of hanging nodes (hn) corresponding to $\gamma = 0.53$ (a) hn $= 2$ (b) hn $= 6$ (c) hn $= 10$

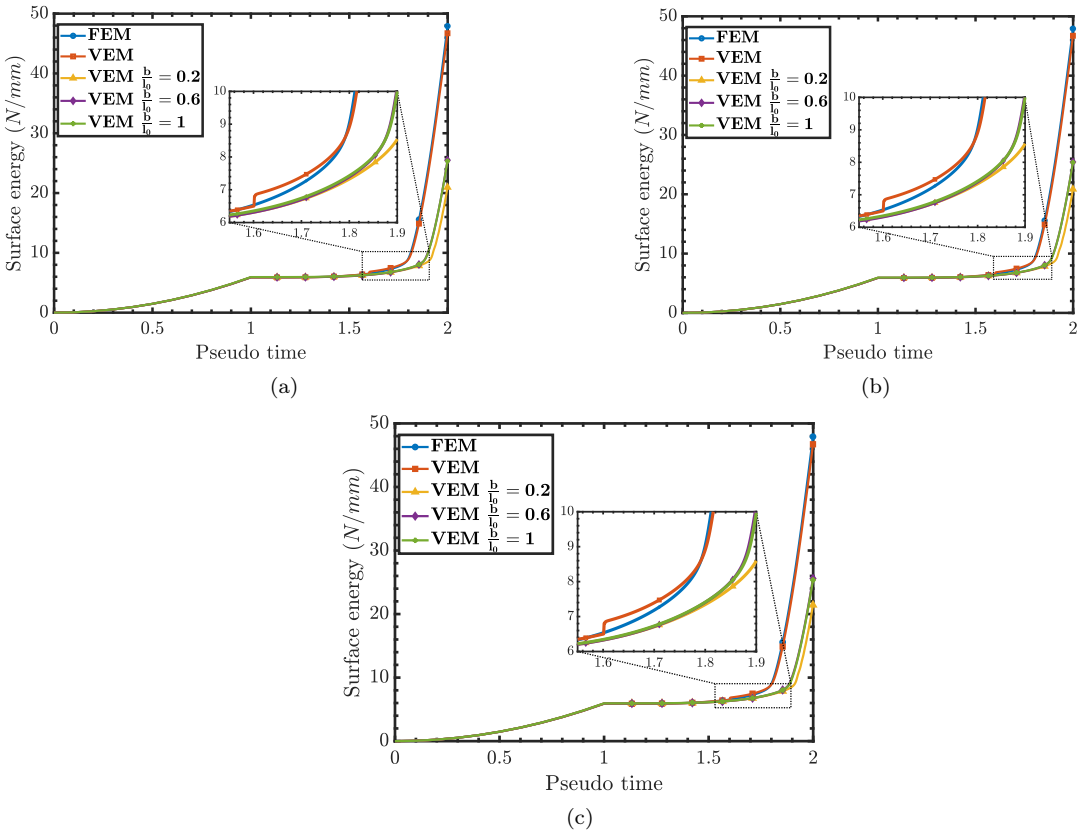

Figure 28: Surface energies for various values of b/l_0 ratios for different number of hanging nodes (hn) corresponding to $\gamma = 1$ (a) hn = 2 (b) hn = 6 (c) hn = 10

4.3. Symmetric three-point bend test

Next, the problem of a three-point bend specimen subjected to a symmetrically applied vertical displacement from the top is considered. Fig. 29 shows the schematic of the specimen and loading conditions. The elastic and fracture material properties are taken from [37], with $\lambda = 12000\ \mathrm{N}/mm^2$, $\mu = 8000\ \mathrm{N}/mm^2$, $G_c = 0.5\ \mathrm{N/mm}$ and $l_0 = 0.03$ mm. The size of the mesh near the notch (h_0) is chosen to ensure a l_0/h_0 ratio of 8. A total vertical downwward displacement of 0.01 mm is applied at the center. The specimen is hinged at the lower left corner and is constrained to move horizontally in the lower right corner. Plane strain condition is assumed.

Fig. 30 shows the virtual element mesh (VEM HN) used in the simulation, which consists of 4-noded quadrilateral elements and 10-noded polygon elements. This enables a rapid transition from the fine mesh to coarse mesh regions. Table 3 shows a comparison of the number of elements used in three different discretization schemes with nSFEM discretization referring to the polygonal smoothed finite element method as employed in [31]. The number of elements can be significantly reduced by up to 42 % for the VEM HN mesh with respect to the CPE4 mesh used in conventional finite elements. This reduction is roughly twice as large than the reduction achieved with the nSFEM discretization used in [31]. Fig. 31 shows

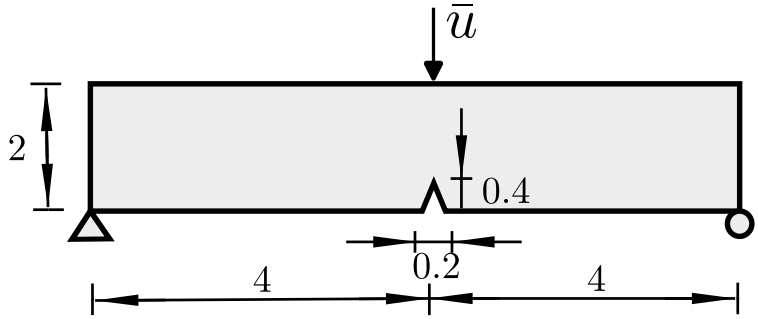

Figure 29: Schematic of the symmetric three-point bend test

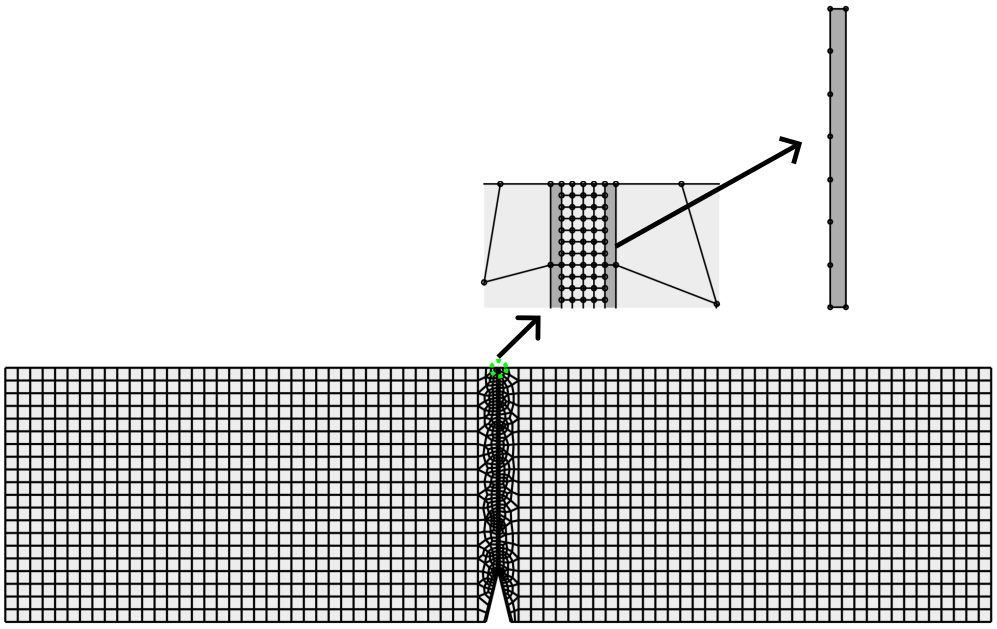

Figure 30: Discretization of the geometry with non matching virtual element mesh (VEM HN). The zoomed in part shows an element with 6 hanging nodes.

the reaction vs applied displacement plots for different discretization schemes. The plots obtained with the VEM HN mesh is compared with the the simulations of [1, 31]. It can be observed that the nSFEM method gives a softer response as compared to voronoi mesh employed in [1], as well as with FEM CPE4 and VEM HN mesh employed in this work. This indicates the superior performance in terms of accuracy and speed of the VEM HN mesh over nSFEM mesh.

Fig. 32 highlights the stages of crack propagation in the specimen with the VEM HN mesh. It can be observed that using elements 10-noded elements, the results obtained are comparable to the FEM mesh and nSFEM mesh as reported in [31]. The crack initiates from the notch which acts as a stress concentrator and propagates vertically upwards until a final failure is achieved.

Table 3: Comparison between number of elements for different discretization schemes

Discretization	Number of elements
FEM CPE4	6548
nSFEM [31]	5132 (**22%** ↓)
VEM HN	3786 (**42%** ↓)

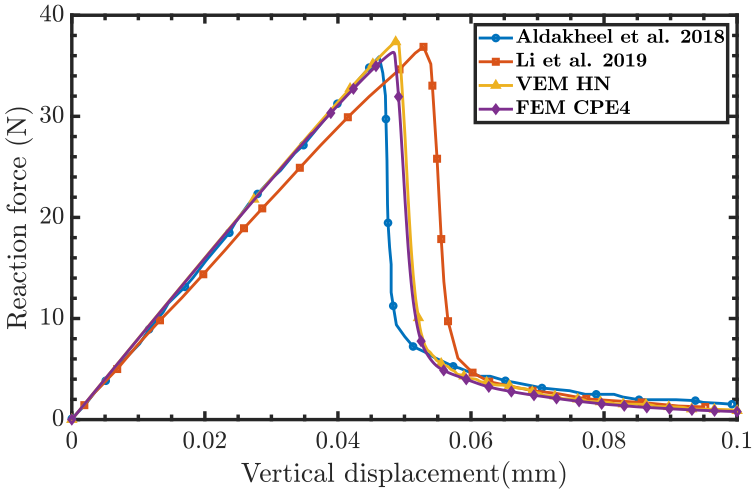

Figure 31: Reaction vs. displacement plot for different types of discretization

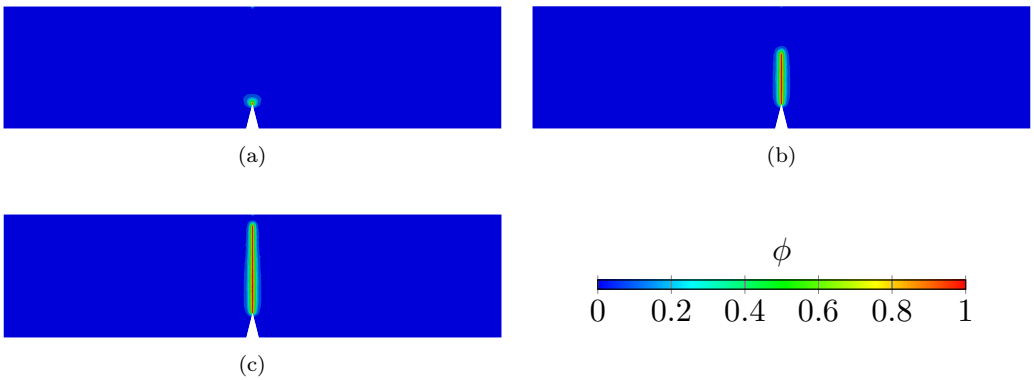

Figure 32: Stages of crack propagation in the three-point bending specimen with VEM HN mesh at displacement (a) $\bar{u} = 0.0049$ mm, (b) $\bar{u} = 0.0052$ mm (c) $\bar{u} = 0.01$ mm

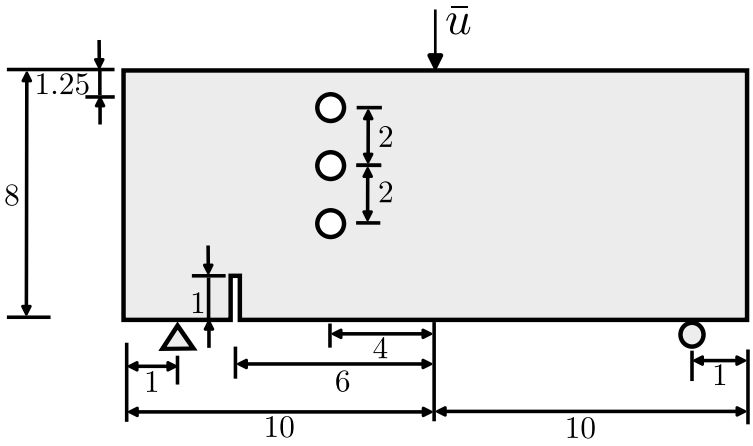

Figure 33: Schematic of the asymmetric three-point bending specimen

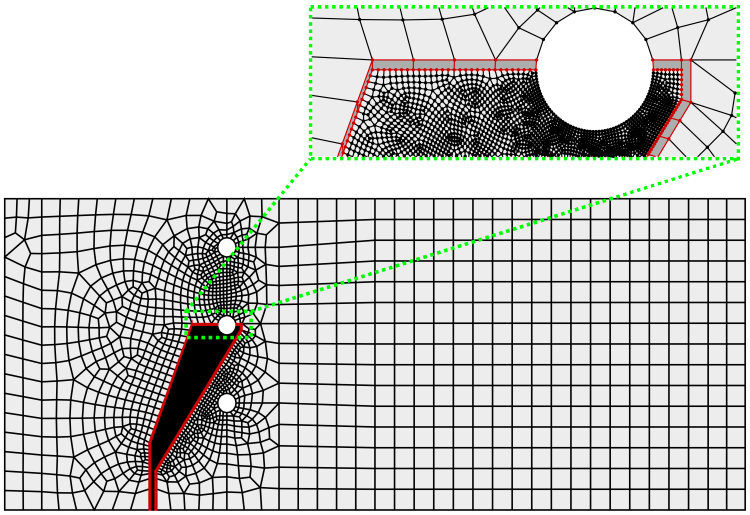

Figure 34: Discretization of the geometry with non matching virtual element mesh. The zoomed in part shows the 10-noded transition elements

4.4. Asymmetric three-point bend test

The crack propagation in the symmetric three-point bend test in Section 4.3 was along a straight line. We now consider the case of the asymmetric three-point bend test, where the crack path no longer remains straight due to the presence of an eccentrically placed notch. A schematic of the geometry and the boundary conditions is shown in Fig. 33. The geometry of the specimen is from the experiments conducted on a PMMA specimen in [7]. The elastic and fracture material parameters for the phase-field fracture simulations are taken from [37], with $\lambda = 12000\text{N}/mm^2$, $\mu = 8000\text{N}/mm^2$, $G_c = 1\text{N}/\text{mm}$ and $l_0 = 0.025\text{mm}$. The simulation is run until a downward vertical displacement of 0.1985 mm, with displacement increments of 1×10^{-3} mm in the first 150 increments, which is subsequently reduced to 1×10^{-3} mm for the remaining increments to capture the brittle crack propagation. Plane strain condition is assumed.

Table 4: Comparison between number of elements for different discretization schemes

Discretization	Number of elements
FEM [37]	58000
VEM [10]	17200
VEM HN	17042

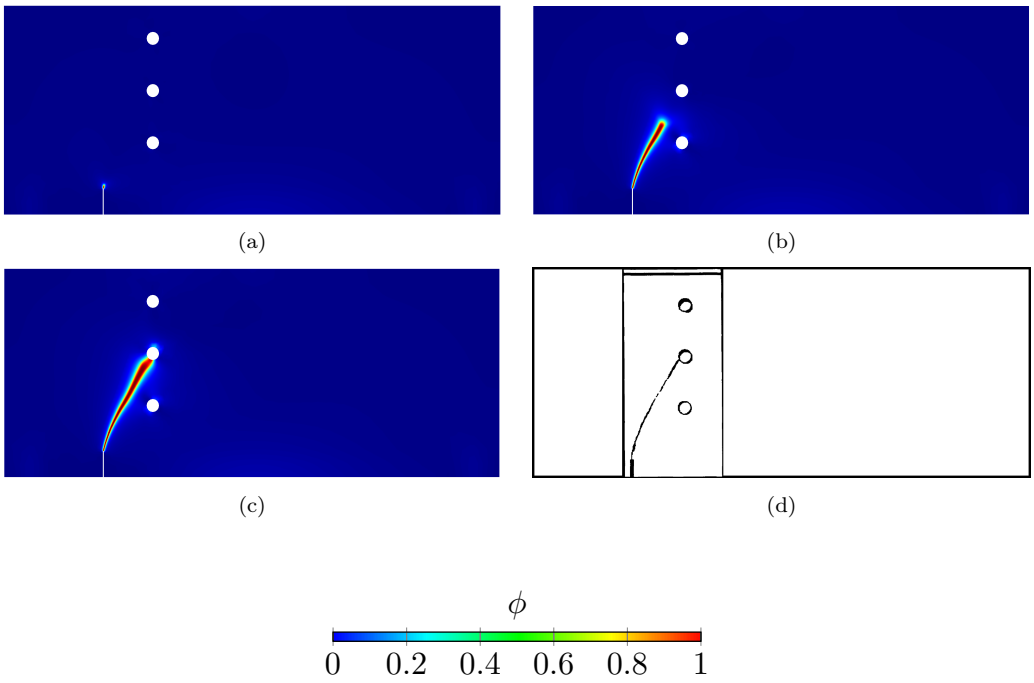

Figure 35: Stages of crack propagation in the asymmetric three-point bending specimen with VEM HN mesh at displacement (a) $\bar{u} = 0.172$ mm, (b) $\bar{u} = 0.198$ mm (c) $\bar{u} = 0.1985$ mm (d) Experimental crack pattern [7]

Fig. 34 illustrates the virtual element mesh (VEM HN) employed in the simulation. A fine mesh is used in the region where crack propagation is anticipated, and 10-noded transition elements facilitate a rapid transition from the refined mesh region to a coarse mesh. It can be observed that at certain locations we have used virtual elements with a very high aspect ratio (≈ 44). The ratio l_0/h_0 in the pre-refined region is maintained at 2, consistent with [37]. Table 4 compares the number of elements used in the FEM and VEM discretization schemes. Assuming that the number of nodes in the triangular FEM mesh from [37] is approximately half the number of elements, the VEM HN mesh achieves roughly a 40% reduction in degrees of freedom. The VEM mesh presented in [10] contains approximately the same number of elements; however, it employs a J_k-integral fracture criterion [27] combined with an element-splitting technique, potentially resulting in additional nodes.

Fig. 35 highlights the stages of crack propagation. The presence of an asymmetrically

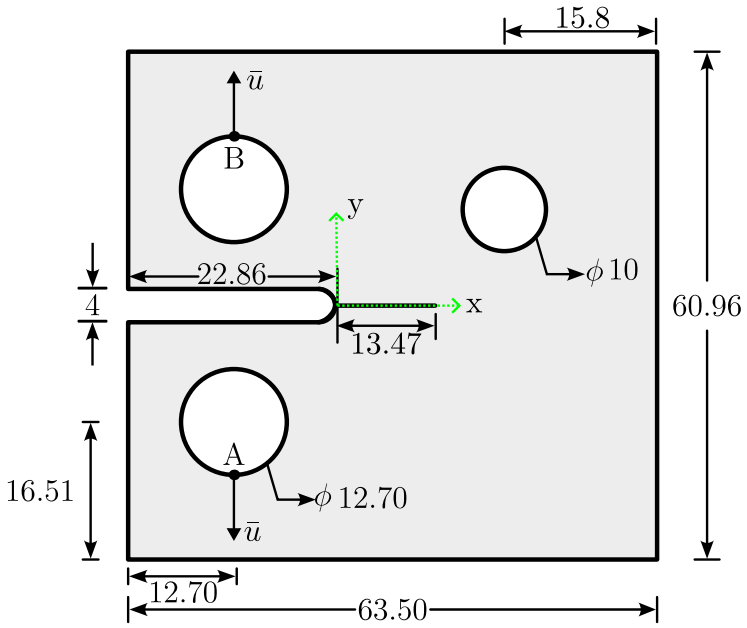

Figure 36: Schematic of the CTS specimen

placed notch and holes creates a mixed-mode loading conditions at the crack tip. As a result, the crack initiates from the notch and starts following a curved path until it reaches the second hole. Even with the presence of transition elements with high aspect ratios, no convergence difficulties were encountered, and the crack path obtained was comparable to the experimental crack patterns in [7], as shown in Fig. 35d.

4.5. Compact Tension Specimen

We now verify the capabilities of the VEM discretization scheme and the refinement strategy proposed in Section 4.2 in predicting accurate crack nucleation and propagation direction with an experiment reported in [43]. In this experiment, a hole is drilled asymmetrically in a compact tension specimen made up of a brittle polymethylmethacrylate (PMMA) sheet and a large pre-existing crack of length 13.47 mm is made near the notch. A schematic of the assembly is shown in Fig. 36. A monotonic displacement loading of 0.2 mm is applied at points A and B. This leads to a mixed mode loading at the crack tip. The elastic and fracture material properties were taken from [43] with E = 2980 N/mm^2, $\nu = 0.3$, $G_c = 0.285$ N/mm and $l_0 = 0.1$ mm.

We analyse this problem using the following three different meshing strategies:

- VEM VORO: The CTS domain is discretised with a Voronoi mesh consisting of polygons with the number of sides ranging from 4 to 9.
- VEM HN: The CTS domain is discretised with 10-noded virtual elements placed atleast at a distance of $0.6l_0$ from the crack front.

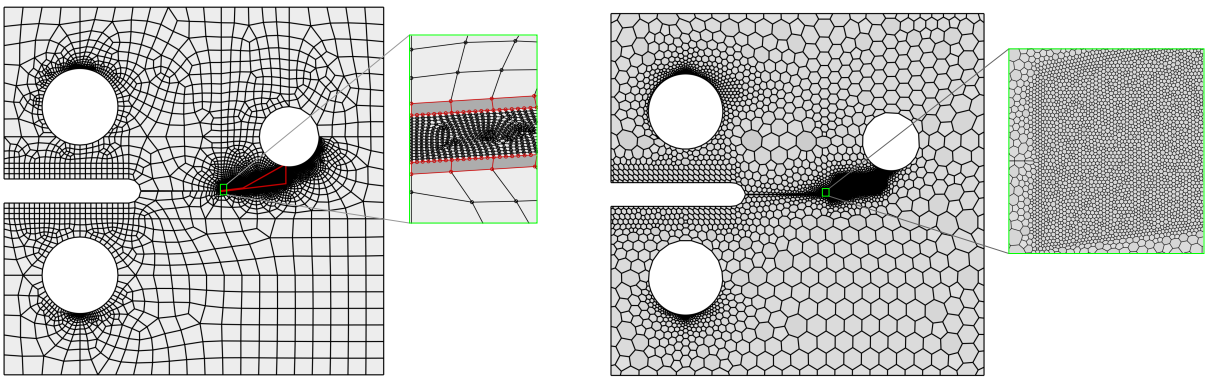

(a) (b)

Figure 37: (a) VEM HN mesh (the zoomed-in part shows the mesh with 6 hanging nodes) (b) VEM VORO mesh

- VEM SAMR: The CTS domain is discretised using a Static Adaptive Mesh Refinement Strategy (SAMR). We use the term "Static" to imply that after a certain criterion is met, the mesh is manually refined in a region around the crack front. This strategy can be used for cases when the crack path is not known *a priori*.

The VEM HN and the VEM VORO mesh are shown in Fig. 37a and Fig. 37b respectively. In both cases, the mesh is pre-refined in the regions where the crack is expected to propagate. Fig. 38 shows the flow chart describing the VEM SAMR strategy, where the simulation is first run on a coarse mesh, until a maximum phase-field value of 0.4 is reached in any node of the mesh. After this stage, the simulation is stopped, and the expected crack front is identified by looking at the phase-field gradients. Then, the crack front region is meshed using the strategies developed in Section 4.2. While refining we keep a fine mesh until a distance of atleast $1l_0$ from the crack front and use no more than six hanging nodes. The meshing is done using the ABAQUS CAE pre-processor, while the transition elements are generated using an in-house developed MATLAB code. Adjustments are then made to the adjoining coarse mesh and the final refined mesh is generated. The refined mesh will have new nodes and the ABAQUS input file feature `*MAP SOLUTION*` is used to map the coarse mesh solution to the fine mesh. The simulation is continued until the crack reaches the end of the pre-refined zone, at which stage the solution at the last increment is stored, and the analysis is terminated. The process is continued for the entire loading history. The mesh size near the notch (h_0) in each of the meshes is taken to be around $l_0/10$ to $l_0/12.5$.

Fig 39 shows the phase-field damage contour in the pre-refined VEM HN and VEM VORO mesh. The crack initiates from the pre-existing crack and curves upwards, until it reaches the asymmetrically placed hole. A similar trend is observed for the VEM SAMR mesh, where a few meshes used in the refinement step are shown in Fig. 40. A zoomed-in region of the mesh along with the phase-field contour is also shown in each of these figures. We initiate the refinement procedure when the phase-field value reaches a value of around 0.4 at any node. This is evident from Fig. 40a, where the initial coarse mesh has 2503 nodes. Fig. 40b shows the 1^{st} refinement stage, where the mesh is refined till a distance of $\pm 0.6l_0$

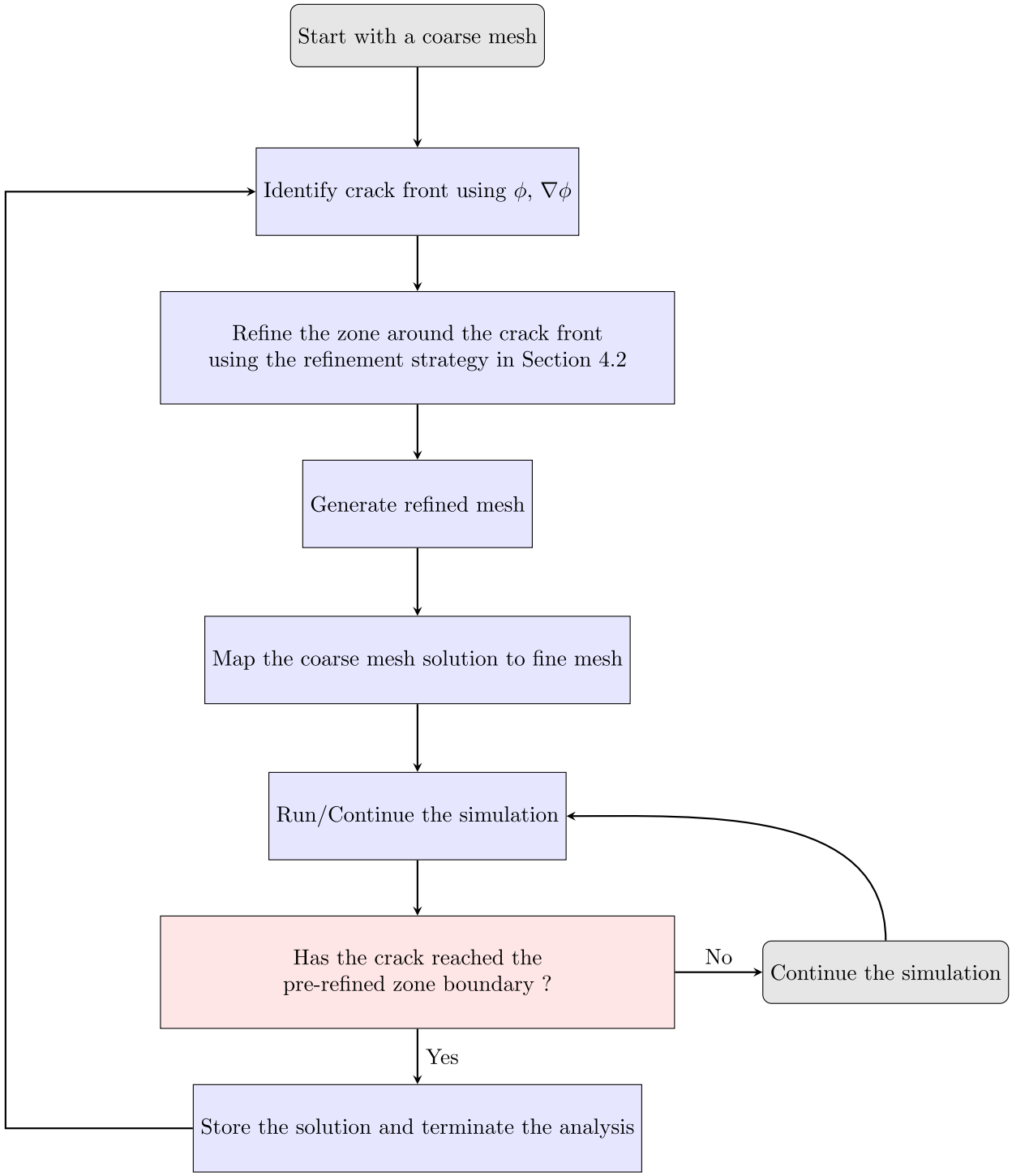

Figure 38: Flowchart for the SAMR strategy implemented in ABAQUS v6.14

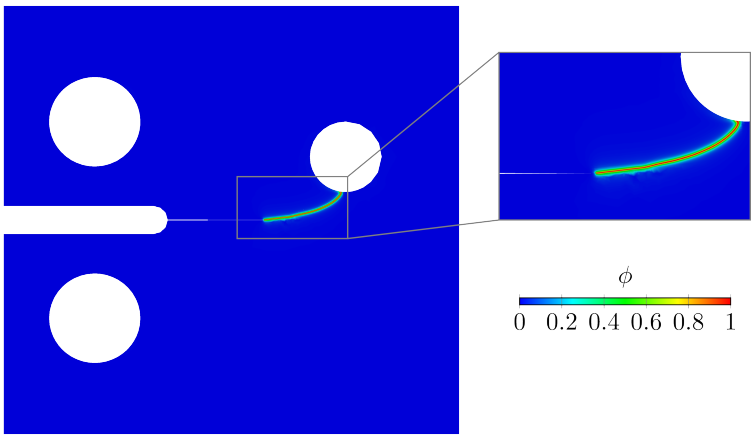

Figure 39: Contours of the crack phase-field for the VEM HN and VEM VORO meshes.

from the crack front and 10-noded elements are used to transition from the fine mesh to the coarse mesh. Fig. 40c, 40d show the subsequent refinement stages. The final refined mesh is shown in Fig. 40e which has about 24732 nodes. This is about a 15 percent reduction as compared to the pre-refined mesh shown in Fig. 37a. The final crack path of the SAMR mesh is plotted along with the pre-refined mesh Fig. 41. It can be observed that though the crack path obtained with the VEM HN, VEM VORO and VEM SAMR mesh coincides with the numerical simulations done with an FEM mesh in [43], a slight difference can be seen with respect to the experimentally observed crack patterns for both VEM and FEM simulations.

The reaction force (obtained at the loading point) vs. the crack opening displacement (COD) is shown in Fig. 42a. The COD is measured at the load points on the notch face. It can be observed that the VEM HN, VEM VORO and VEM SAMR mesh have similar peak load (around 22 N) as compared to the experimental results and numerical simulations using FEM in [43]. The error in the computation of peak vertical reaction obtained with the VEM HN mesh with respect to the experiment is 6.3 percent as compared to 7.8 percent for the FEM mesh used in [43]. Consequently, the VEM HN mesh shows lesser energy dissipation as compared to the FEM mesh. This is also reflected in the post-peak response. This observation could be explained using Fig. 17 and Fig. 25 where it was shown that the surface energy was underpredicted in mixed mode fracture simulations due to the presence of hanging nodes. Fig. 42b shows the effect of increasing l_0/h_0 ratio, which was achieved with increasing levels mesh refinements keeping l_0 fixed. The presence of hanging nodes facilitated a mesh refinement of size $l_0/25$ near the crack tip without leading to an exorbitant increase in computational cost. It can be observed that the peak load successively gets closer to the experimentally measured peak load with increasing l_0/h_0 value. While this emphasizes the strength of classical phase-field models in accurately predicting crack nucleation under mixed-mode loading conditions, it also highlights a key limitation: the need for a very fine mesh to capture the correct crack nucleation load.

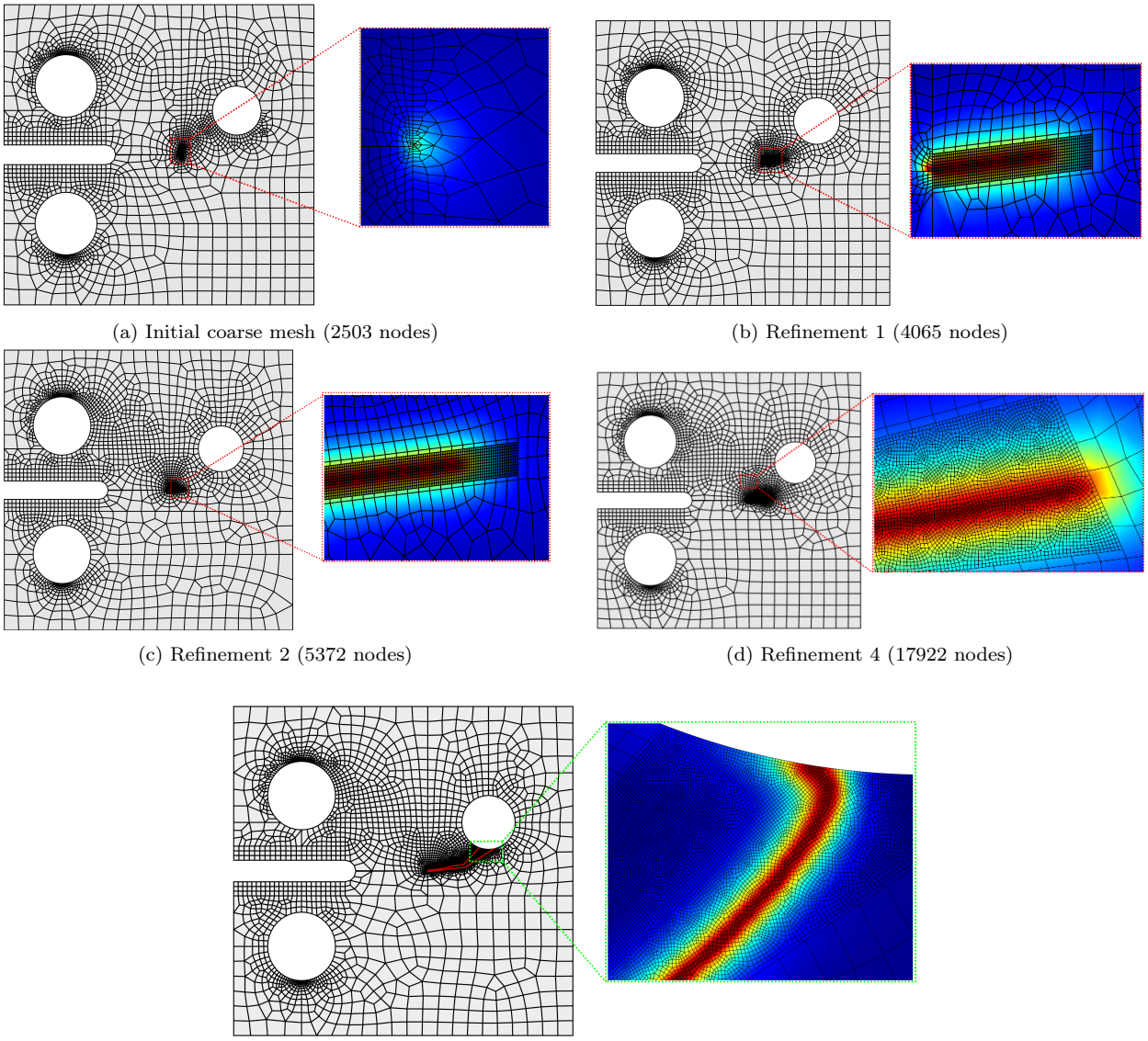

(a) Initial coarse mesh (2503 nodes)

(b) Refinement 1 (4065 nodes)

(c) Refinement 2 (5372 nodes)

(d) Refinement 4 (17922 nodes)

(e) Final mesh in refinement 6, the regions marked with red in the figure on left show the final mesh around which hanging nodes were introduced (24732 nodes)

Figure 40: Meshes used in the refinement scheme and the phase-field contours plotted near the crack vicinity

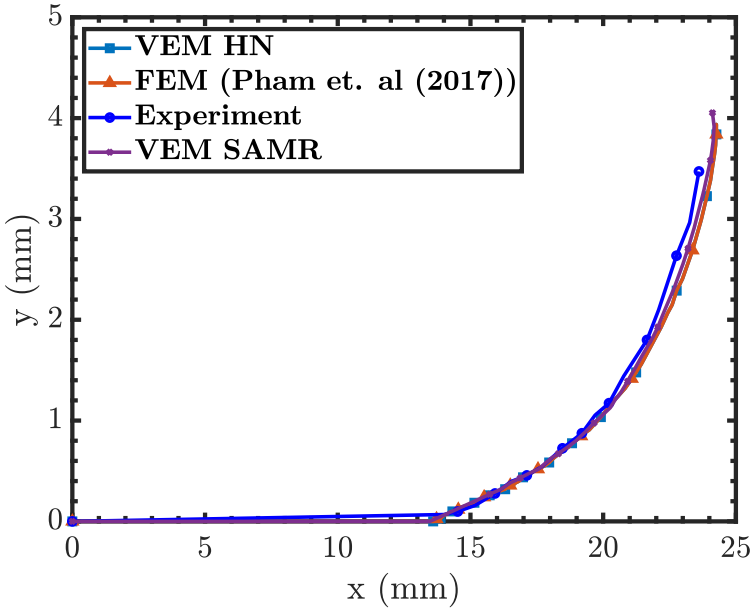

Figure 41: Comparison of crack paths, the x and y distance are with respect to the origin placed at the notch as shown in Fig 36

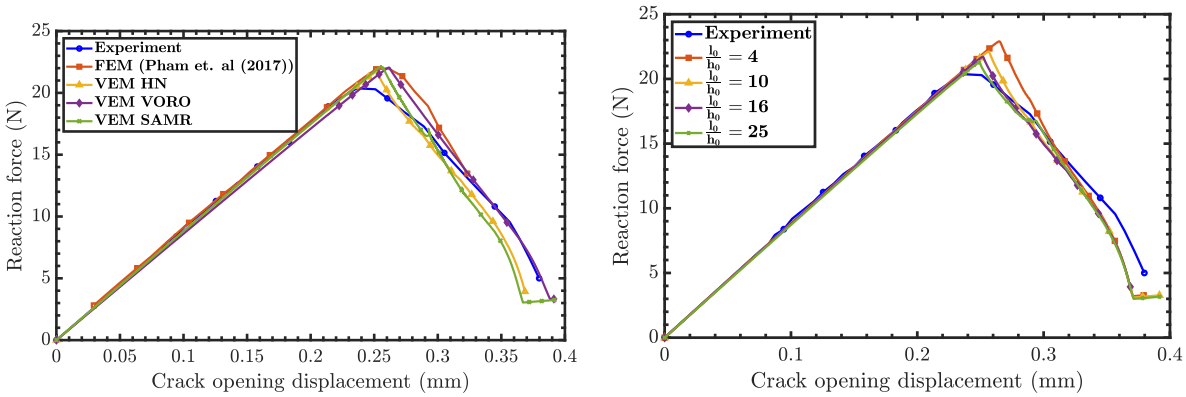

Figure 42: Comparisons between the experimental and FEM results of [43] with VEM results, (a) Reaction force vs. COD (b) Effect of l_0/h_0 ratio on reaction vs COD curves.

5. Conclusion

In this work, we present a robust and efficient VEM discretization for the phase-field brittle damage model, highlighting VEM's flexibility in accommodating elements with multiple hanging nodes for seamless transitions between fine and coarse mesh regions. A strategy was developed to set some guidelines for fixing the number and positioning of hanging nodes using analytical insights from linear elastic fracture mechanics (LEFM). The key findings are as follows:

- Employing an excessive number of hanging nodes within a single element can introduce inaccuracies in the global response during phase-field fracture simulations. However, if the element size is maintained within a reasonable limit, increasing the number of hanging nodes results in relatively minor errors ($< 2\%$) in the reaction force and displacement at failure. On the other hand, the error in the peak stress near the crack tip and the dissipated surface energy can become significant, depending on the positioning of these hanging nodes relative to the crack front. Consequently, this can substantially influence the post-peak behavior of the simulated structure.

- The fracture surface energy is under-predicted in mixed-mode fracture simulations when elements with hanging nodes are used. This can lead to differences in the post-peak fracture response as compared to conventional FEM.

- The virtual elements with hanging nodes should be placed at least at a distance of $\pm 0.6 l_0$ from the crack front to minimize loss of accuracy. The number of hanging nodes in mesh transition can be used in the range of 6 to 10 near the crack front to achieve a balance between accuracy and computational cost.

- The proposed refinement strategy reduced CPU time by up to 56 % compared to FEM with conforming elements, without compromising accuracy in peak load predictions and crack path evolution, and can reduce the degrees of freedom by at least 60% if the transition elements with hanging nodes are strategically placed.

- In terms of degrees of freedom, our approach outperformed the nSFEM [31], showing efficiency gains.

- Experimental validation demonstrated a good correlation with the crack patterns observed in the asymmetric three-point bend test and CTS specimen under mixed-mode I+II loading conditions.

- A Static Adaptive Mesh Refinement (SAMR) strategy is also proposed that implements the refinement guidelines proposed in an adaptive framework. Its implementation in the commercial software ABAQUS can potentially lead to large-scale commercial adoption for phase-field fracture simulations when the crack path is not known *a priori*.

These insights underscore the potential of this approach to design efficient adaptive mesh refinement (AMR) strategies and enable accurate phase-field fracture modeling for large-scale structures. Additionally, the implementation of this method within the commercial software Abaqus enhances its potential for industry adoption, allowing for scalable and efficient crack propagation simulations in complex engineering applications. Furthermore, the proposed technique can be readily extended to study crack propagation in heterogeneous structures.

References

[1] Aldakheel, F., Hudobivnik, B., Hussein, A., Wriggers, P., 2018. Phase-field modeling of brittle fracture using an efficient virtual element scheme. Computer Methods in Applied Mechanics and Engineering 341, 443–466.

[2] Aldakheel, F., Noii, N., Wick, T., Allix, O., Wriggers, P., 2021. Multilevel global–local techniques for adaptive ductile phase-field fracture. Computer Methods in Applied Mechanics and Engineering 387, 114175.

[3] Ambati, M., Gerasimov, T., De Lorenzis, L., 2015. A review on phase-field models of brittle fracture and a new fast hybrid formulation. Computational Mechanics 55, 383–405.

[4] Badnava, H., Msekh, M.A., Etemadi, E., Rabczuk, T., 2018. An h-adaptive thermo-mechanical phase field model for fracture. Finite Elements in Analysis and Design 138, 31–47.

[5] Barenblatt, G.I., 1962. The mathematical theory of equilibrium cracks in brittle fracture. Advances in applied mechanics 7, 55–129.

[6] Benedetto, M.F., Caggiano, A., Etse, G., 2018. Virtual elements and zero thickness interface-based approach for fracture analysis of heterogeneous materials. Computer Methods in Applied Mechanics and Engineering 338, 41–67.

[7] Bittencourt, T.N., Wawrzynek, P.A., Ingraffea, A.R., Sousa, J., 1996. Quasi-automatic simulation of crack propagation for 2d lefm problems. Engineering Fracture Mechanics 55, 321–334.

[8] Bourdin, B., Francfort, G.A., Marigo, J.J., 2000. Numerical experiments in revisited brittle fracture. Journal of the Mechanics and Physics of Solids 48, 797–826.

[9] Cascio, M.L., Milazzo, A., Benedetti, I., 2020. Virtual element method for computational homogenization of composite and heterogeneous materials. Composite Structures 232, 111523.

[10] Chen, Y., Sun, D., Perego, U., Li, Q., 2025. Brittle crack propagation simulation based on the virtual element method and jk-integral fracture criterion. Engineering Fracture Mechanics 314, 110684.

[11] Cheng, P., Zhuang, X., Zhu, H., Fish, J., 2023. Application of s-version finite element method to phase field modeling for localized fractures. Computers and Geotechnics 156, 105204.

[12] Chi, H., Da Veiga, L.B., Paulino, G.H., 2017. Some basic formulations of the virtual element method (vem) for finite deformations. Computer Methods in Applied Mechanics and Engineering 318, 148–192.

[13] Cihan, M., Hudobivnik, B., Korelc, J., Wriggers, P., 2022. A virtual element method for 3d contact problems with non-conforming meshes. Computer Methods in Applied Mechanics and Engineering 402, 115385.

[14] Da Veiga, L.B., Brezzi, F., Marini, L.D., 2013. Virtual elements for linear elasticity problems. SIAM Journal on Numerical Analysis 51, 794–812.

[15] Da Veiga, L.B., Lovadina, C., Mora, D., 2015. A virtual element method for elastic and inelastic problems on polytope meshes. Computer methods in applied mechanics and engineering 295, 327–346.

[16] Das, S., Sharma, S., Ramaswamy, A., Roy, D., Reddy, J., 2021. A geometrically inspired model for brittle damage in compressible elastomers. Journal of Applied Mechanics 88, 081002.

[17] Dassault Systèmes Simulia Corp., 2013. Abaqus/Standard User's Manual, Version 2024. Providence, RI, USA.

[18] De Bellis, M.L., Wriggers, P., Hudobivnik, B., Zavarise, G., 2018. Virtual element formulation for isotropic damage. Finite Elements in Analysis and Design 144, 38–48.

[19] Francfort, G.A., Marigo, J.J., 1998. Revisiting brittle fracture as an energy minimization problem. Journal of the Mechanics and Physics of Solids 46, 1319–1342.

[20] Frémond, M., Nedjar, B., 1996. Damage, gradient of damage and principle of virtual power. International journal of solids and structures 33, 1083–1103.

[21] Gain, A.L., Talischi, C., Paulino, G.H., 2014. On the virtual element method for three-dimensional linear elasticity problems on arbitrary polyhedral meshes. Computer Methods in Applied Mechanics and Engineering 282, 132–160.

[22] Gatta, C., Pingaro, M., Addessi, D., Trovalusci, P., 2024. A coupled virtual element-interface model for analysis of fracture propagation in polycrystalline composites. Computer Methods in Applied Mechanics and Engineering 432, 117383.

[23] Gerasimov, T., Noii, N., Allix, O., De Lorenzis, L., 2018. A non-intrusive global/local approach applied to phase-field modeling of brittle fracture. Advanced modeling and simulation in engineering sciences 5, 1–30.

[24] Hirshikesh, H., Pramod, A., Waisman, H., Natarajan, S., 2021. Adaptive phase field method using novel physics based refinement criteria. Computer Methods in Applied Mechanics and Engineering 383, 113874.

[25] Huang, Y.j., Zheng, Z.s., Yao, F., Zeng, C., Zhang, H., Natarajan, S., Xu, S.l., 2024. Arbitrary polygon-based csfem-pfczm for quasi-brittle fracture of concrete. Computer Methods in Applied Mechanics and Engineering 424, 116899.

[26] Hussein, A., Hudobivnik, B., Wriggers, P., 2020. A combined adaptive phase field and discrete cutting method for the prediction of crack paths. Computer Methods in Applied Mechanics and Engineering 372, 113329.

[27] Kienzler, R., Herrmann, G., 1997. On the properties of the eshelly tensor. Acta Mechanica 125, 73–91.

[28] Kristensen, P.K., Niordson, C.F., Martínez-Pañeda, E., 2021. An assessment of phase field fracture: crack initiation and growth. Philosophical Transactions of the Royal Society A 379, 20210021.

[29] Kuhn, C., Schlüter, A., Müller, R., 2015. On degradation functions in phase field fracture models. Computational Materials Science 108, 374–384.

[30] Kumar, P., 2009. Elements of Fracture Mechanics. McGraw-Hill Education (India) Private Limited. URL: https://books.google.co.in/books?id=hOkpf0tqnFUC.

[31] Li, S., Cui, X., 2020. N-sided polygonal smoothed finite element method (nsfem) with non-matching meshes and their applications for brittle fracture problems. Computer Methods in Applied Mechanics and Engineering 359, 112672.

[32] Liu, G., Dai, K., Nguyen, T., 2007. A smoothed finite element method for mechanics problems. Computational Mechanics 39, 859–877.

[33] Liu, T.R., Aldakheel, F., Aliabadi, M., 2023. Virtual element method for phase field modeling of dynamic fracture. Computer Methods in Applied Mechanics and Engineering 411, 116050.

[34] Liu, T.R., Aldakheel, F., Aliabadi, M., 2024. Hydrogen assisted cracking using an efficient virtual element scheme. Computer Methods in Applied Mechanics and Engineering 420, 116708.

[35] Lo, Y.S., Hughes, T.J., Landis, C.M., 2023. Phase-field fracture modeling for large structures. Journal of the Mechanics and Physics of Solids 171, 105–118.

[36] Mengolini, M., Benedetto, M.F., Aragón, A.M., 2019. An engineering perspective to the virtual element method and its interplay with the standard finite element method. Computer Methods in Applied Mechanics and Engineering 350, 995–1023.

[37] Miehe, C., Hofacker, M., Welschinger, F., 2010. A phase field model for rate-independent crack propagation: Robust algorithmic implementation based on operator splits. Computer Methods in Applied Mechanics and Engineering 199, 2765–2778.

[38] Navidtehrani, Y., Duddu, R., Martínez-Pañeda, E., 2024. Damage mechanics challenge: Predictions based on the phase field fracture model. Engineering Fracture Mechanics 301, 110046.

[39] Nguyen-Thanh, V.M., Zhuang, X., Nguyen-Xuan, H., Rabczuk, T., Wriggers, P., 2018. A virtual element method for 2d linear elastic fracture analysis. Computer Methods in Applied Mechanics and Engineering 340, 366–395.

[40] Noii, N., Aldakheel, F., Wick, T., Wriggers, P., 2020. An adaptive global–local approach for phase-field modeling of anisotropic brittle fracture. Computer Methods in Applied Mechanics and Engineering 361, 112744.

[41] Patil, R., Mishra, B., Singh, I., 2018. An adaptive multiscale phase field method for brittle fracture. Computer Methods in Applied Mechanics and Engineering 329, 254–288.

[42] Peng, F., Liu, H., Li, S., Cui, X., 2022. Quadtree-polygonal smoothed finite element method for adaptive brittle fracture problems. Engineering Analysis with Boundary Elements 134, 491–509.

[43] Pham, K., Ravi-Chandar, K., Landis, C., 2017. Experimental validation of a phase-field model for fracture. International Journal of Fracture 205, 83–101.

[44] Popp, A., Gitterle, M., Gee, M.W., Wall, W.A., 2010. A dual mortar approach for 3d finite deformation contact with consistent linearization. International Journal for Numerical Methods in Engineering 83, 1428–1465.

[45] Pramod, A., Annabattula, R., Ooi, E., Song, C., Natarajan, S., et al., 2019. Adaptive phase-field modeling of brittle fracture using the scaled boundary finite element method. Computer Methods in Applied Mechanics and Engineering 355, 284–307.

[46] Reis, F., Pires, F.A., 2014. A mortar based approach for the enforcement of periodic boundary conditions on arbitrarily generated meshes. Computer Methods in Applied Mechanics and Engineering 274, 168–191.

[47] Rivarola, F.L., Labanda, N., Benedetto, M., Etse, G., 2020. A virtual element and interface based concurrent multiscale method for failure analysis of quasi brittle heterogeneous composites. Computers & Structures 239, 106338.

[48] Santillán, D., Mosquera, J.C., Cueto-Felgueroso, L., 2017. Phase-field model for brittle fracture. validation with experimental results and extension to dam engineering problems. Engineering Fracture Mechanics 178, 109–125.

[49] Si, Z., Yu, T., Li, Y., Natarajan, S., 2023. Adaptive multi-patch isogeometric phase-field method for quasi-static brittle fracture based on nitsche's method. Computer Methods in Applied Mechanics and Engineering 414, 116154.

[50] Si, Z., Yu, T., Natarajan, S., et al., 2024. An adaptive multi-patch isogeometric phase-field model for dynamic brittle fracture. Computers & Mathematics with Applications 153, 1–19.

[51] Strang, G., 1973. Piecewise polynomials and the finite element method. Bulletin of the American Mathematical Society 79, 1128 – 1137.

[52] Sukumar, N., Bolander, J.E., 2022. Virtual element method for modeling the deformation of multiphase composites. Mechanics Research Communications 124, 103907.

[53] Sukumar, N., Moës, N., Moran, B., Belytschko, T., 2000. Extended finite element method for three-dimensional crack modelling. International journal for numerical methods in engineering 48, 1549–1570.

[54] Sukumar, N., Tabarraei, A., 2004. Conforming polygonal finite elements. International Journal for Numerical Methods in Engineering 61, 2045–2066.

[55] Surendran, M., Lee, C., Nguyen-Xuan, H., Liu, G., Natarajan, S., 2021. Cell-based smoothed finite element method for modelling interfacial cracks with non-matching grids. Engineering Fracture Mechanics 242, 107476.

[56] Tabarraei, A., Sukumar, N., 2005. Adaptive computations on conforming quadtree meshes. Finite elements in Analysis and Design 41, 686–702.

[57] Beirão da Veiga, L., Brezzi, F., Cangiani, A., Manzini, G., Marini, L.D., Russo, A., 2013. Basic principles of virtual element methods. Mathematical Models and Methods in Applied Sciences 23, 199–214.

[58] Beirão da Veiga, L., Brezzi, F., Marini, L.D., Russo, A., 2014. The hitchhiker's guide to the virtual element method. Mathematical models and methods in applied sciences 24, 1541–1573.

[59] Wijesinghe, D.R., Natarajan, S., You, G., Khandelwal, M., Dyson, A., Song, C., Ooi, E.T., 2023. Adaptive phase-field modelling of fracture propagation in poroelastic media using the scaled boundary finite element method. Computer Methods in Applied Mechanics and Engineering 411, 116056.

[60] Wohlmuth, B.I., 2000. A mortar finite element method using dual spaces for the lagrange multiplier. SIAM journal on numerical analysis 38, 989–1012.

[61] Wriggers, P., Rust, W.T., Reddy, B., 2016. A virtual element method for contact. Computational Mechanics 58, 1039–1050.

[62] Wu, J.Y., Huang, Y., Zhou, H., Nguyen, V.P., 2021. Three-dimensional phase-field modeling of mode i+ ii/iii failure in solids. Computer Methods in Applied Mechanics and Engineering 373, 113537.

[63] Zhang, H., Wu, J., Lv, J., 2012. A new multiscale computational method for elastoplastic analysis of heterogeneous materials. Computational mechanics 49, 149–169.

[64] Zhang, H.W., Wu, J.K., Lü, J., Fu, Z.D., 2010. Extended multiscale finite element method for mechanical analysis of heterogeneous materials. Acta mechanica sinica 26, 899–920.